

Old Dominion University

## ODU Digital Commons

---

Electrical & Computer Engineering Theses &  
Dissertations

Electrical & Computer Engineering

---

Spring 2009

### A Compact Lidar for Aircraft Ozone Atmospheric Measurements

Joel A. Marcia  
*Old Dominion University*

Follow this and additional works at: [https://digitalcommons.odu.edu/ece\\_etds](https://digitalcommons.odu.edu/ece_etds)



Part of the [Aeronautical Vehicles Commons](#), [Atmospheric Sciences Commons](#), [Power and Energy Commons](#), [Remote Sensing Commons](#), and the [Systems Architecture Commons](#)

---

#### Recommended Citation

Marcia, Joel A.. "A Compact Lidar for Aircraft Ozone Atmospheric Measurements" (2009). Master of Science (MS), Thesis, Electrical & Computer Engineering, Old Dominion University, DOI: 10.25777/4xh0-zg16  
[https://digitalcommons.odu.edu/ece\\_etds/424](https://digitalcommons.odu.edu/ece_etds/424)

This Thesis is brought to you for free and open access by the Electrical & Computer Engineering at ODU Digital Commons. It has been accepted for inclusion in Electrical & Computer Engineering Theses & Dissertations by an authorized administrator of ODU Digital Commons. For more information, please contact [digitalcommons@odu.edu](mailto:digitalcommons@odu.edu).

# A COMPACT LIDAR FOR AIRCRAFT OZONE ATMOSPHERIC MEASUREMENTS

by

Joel A. Marcia  
B.S.E.E. May 2007, Old Dominion University

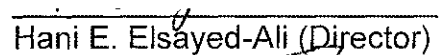
A Thesis submitted to the Faculty of Old Dominion University in Partial  
Fulfillment of the Requirement for the Degree of

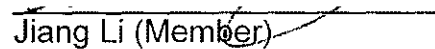
MASTER OF SCIENCE

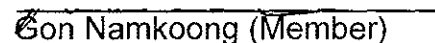
ELECTRICAL ENGINEERING

OLD DOMINION UNIVERSITY  
MAY 2009

Approved by:

  
Hani E. Elsayed-Ali (Director)

  
Jiang Li (Member)

  
Gon Namkoong (Member)

## **Abstract**

### **A COMPACT LIDAR FOR AIRCRAFT OZONE ATMOSPHERIC MEASUREMENTS**

Joel A. Marcia  
Old Dominion University, 2009  
Director: Dr. Hani E. Elsayed-Ali

Researchers and the general public have expressed great concern over how human activities exacerbate pollution's deteriorating impact upon the environment. Effects such as global warming, air quality and ozone layer depletion are but a few examples that can have a dramatic effect on the quality of life worldwide.

A compact lidar system for the purpose of aircraft ozone atmospheric measurements was tested and evaluated. This system will eventually be deployed for aircraft-based, and possibly unpiloted atmospheric vehicle (UAV), ozone and aerosol measurements to improve our understanding of ozone production and transport. Each of the major subsystems was characterized and from the results the subsystems were optimized for maximum operational efficiency. Furthermore, atmospheric testing was conducted by transmitting the 527-nm visible beam into the atmosphere and the backscattered results were compared to the theoretical results of the lidar equation.

Co-Director of Advisory Committee: Dr. Russell J. De Young

This thesis is dedicated to the One who is the source of all knowledge.

## ACKNOWLEDGMENTS

I would like to thank my advisor, Dr. Hani Elsayed-Ali, for pointing the way and for giving me the opportunity to pursue the work needed to complete this thesis. Additional thanks and much appreciation to Dr. Russell De Young of NASA Langley Research Center who showed me the way and provided continual support, patience, and hours in guiding my research and editing of this thesis. Both have exemplified the word advisor in every way.

Additionally, I would like to thank all the personnel at the Atmospheric Science Division at NASA Langley Research Center who provided additional help during my research for this thesis.

Also, I would like to thank the members of my committee, Dr. Jiang Li and Dr. Gon Namkoong, that provided the time and effort in serving on the committee.

Last, but not least, I would like to thank my family who provided support in every way, especially my wife Kathleen and daughter Brooke. It has been truly a family affair and I could not have succeeded without them.

## TABLE OF CONTENTS

	Page
LIST OF TABLES .....	viii
LIST OF FIGURES .....	ix
 CHAPTER	
I. INTRODUCTION .....	1
1.1 Ozone .....	2
1.2 Stratospheric Ozone .....	3
1.2.1 Ozone Formation in the stratosphere .....	4
1.2.2 Anthropogenic Destruction of Stratospheric Ozone.....	8
1.3 Tropospheric Ozone .....	10
1.3.1 Ozone Formation in the Troposphere.....	11
1.3.2 Ozone as a Harmful Pollutant.....	13
1.4 Atmospheric Measurements .....	14
1.5 Research Objective.....	18
 II. LIDAR CONCEPTS AND THEORY.....	 19
2.1 Lidar System Architecture .....	19
2.2 Lidar Equation.....	22
2.3 DIAL Equation.....	30
2.4 Frequency Conversion.....	36
2.4.1 Harmonic Generation .....	40
 III. EXPERIMENTAL SETUP.....	 45
3.1 Lidar Transmitter.....	46
3.1.1 Nd:YLF Laser Pump .....	47

	Page
3.1.2 Diode Pumping .....	48
3.1.3 Q-Switching .....	49
3.1.4 Intra-Cavity Frequency Doubling .....	50
3.1.5 Ce:LiCAF Tunable UV Laser Head.....	52
3.1.6 Ce:LiCAF Wavelength Tuning .....	53
3.1.7 Transmitter Optics .....	54
3.2 Receiver System.....	55
3.2.1 Detection Array.....	55
3.3 Lidar Control and Support.....	57
3.4 Data Acquisition System .....	59
3.5 Atmospheric Transmission Setup .....	60
IV. ATMOSPHERIC OZONE LIDAR CALCULATIO .....	62
4.1 Backscatter Coefficients .....	62
4.2 Extinction Coefficient .....	64
4.3 Lidar Calculation .....	66
4.4 DIAL Calculation .....	69
V. LIDAR SYSTEM RESULTS .....	71
5.1 Nd:YLF Pump Laser .....	71
5.2 Fourth Harmonic Generation .....	75
5.3 Receiver Efficiency .....	81
5.4 527-nm Atmospheric Aerosol Test.....	83
VI. DISCUSSION.....	87
VII. CONCLUSIONS.....	94

	Page
REFERENCES.....	96
VITA .....	99



## LIST OF TABLES

Table	Page
1. Lidar equation values .....	68
2. Summary of values used to determine 4th Harmonic generation. ....	80
3. Lidar equation values .....	91

## LIST OF FIGURES

Figure	Page
1. Typical ozone profiles.....	3
2. Ozone hole over Antarctica .....	10
3. Ozone profiles from various instruments .....	16
4. Global map of total ozone by the TOMS satellite .....	17
5. Conceptual illustration of a lidar system .....	20
6. Physical picture of the lidar equation.....	23
7. An illustration of the lidar equation .....	25
8. Absorption cross sections of ozone in the UV spectrum.....	31
9. Energy level diagram illustrating second harmonic generation.....	37
10. 2 <sup>nd</sup> harmonic conversion efficiency based on phase mismatch, $\Delta$ .....	43
11. Block diagram for 2 <sup>nd</sup> and 4 <sup>th</sup> harmonic generation .....	44
12. Ozone lidar system in the lab .....	45
13. A schematic of the lidar system.....	46
14. An optical schematic of the laser transmitter.....	47
15. An optical schematic of the Ce:LiCAF UV laser tunable.....	52
16. Optical schematic of the telescope assembly.....	57
17. Optical schematic of the receiver box.....	57
18. Lidar setup for atmospheric ozone measurements.....	61
19. Theoretical calculation of a lidar return.....	67
20. Calculated DIAL results.....	70

Figure	Page
21. 527-nm laser output vs chiller temperature. ....	72
22. 527-nm laser pump output vs LBO oven temperature .....	73
23. 527-nm laser pump output vs diode current. ....	74
24. 4 <sup>th</sup> harmonic generation vs 527-nm laser pump energy. ....	76
25. 4 <sup>th</sup> harmonic conversion efficiency vs 527-nm pump energy. ....	77
26. Measured/theoretical conversion efficiency.....	79
27. Lidar backscatter results (cloud).....	85
28. Lidar backscatter results (no cloud).....	86
29. Comparison of the theoretical and experimental results.....	92

## CHAPTER I

### INTRODUCTION

In recent years, great concern has escalated over the extent to which human activities pollute the environment. Effects such as global warming, air quality and ozone layer depletion are but a few examples that can have a dramatic affect on the quality of life worldwide. So much so, that legislation has been put forth to make the public aware and to reduce and possibly eliminate the emissions of harmful chemicals into the atmosphere. Ozone is one among several important factors for global warming and air-quality concerns. The quantity and distribution of ozone in the atmosphere have important implications worldwide.

In addition to ozone, atmospheric aerosols, which are minute particles suspended in the atmosphere, have a significant role in the atmosphere and are involved in many atmospheric processes. The aerosols that significantly affect the Earth's climate come from volcanic ash, desert dust, and human activities, such as the burning of coal and oil. While atmospheric aerosols are only minor constituents in the atmosphere, they have a direct influence on the Earth's radiation budget and climate. The direct way is to scatter sunlight directly back into space, which can cool the Earth's surface. The indirect way is by combining with clouds to change the way clouds reflect and absorb sunlight,

---

The journal model used for this thesis is *Optical Engineering*.

which can also lead to cooling the Earth's surface. In addition, atmospheric aerosols can participate in chemical reactions that can instigate the stratospheric ozone's destruction. Furthermore, atmospheric aerosols are recognized as a significant health issue, especially in regards to respiratory ailments such as asthma.

In order to gain a better understanding of ozone, this chapter discusses the mechanisms of ozone formation and destruction along with the factors that affect its concentrations. In addition, the importance of ozone to life on the planet and its effect on living organisms is explained.

## **1.1 Ozone**

Ozone plays a very important role in the atmosphere; however, ozone can be considered a hazardous pollutant depending on the location within the Earth's atmosphere. Ozone is a form of oxygen that is comprised of three oxygen atoms ( $O_3$ ). Oxygen is mostly found in its stable molecular form ( $O_2$ ). Ozone is typically found at two locations in the atmosphere – the stratosphere and the troposphere. In the stratosphere, ozone is beneficial; however, in the troposphere, ozone is detrimental. Figure 1 illustrates typical atmospheric ozone profiles obtained from SAGE II satellite measurements showing the peak stratospheric ozone occurs between 18 and 25 Km depending on latitude.

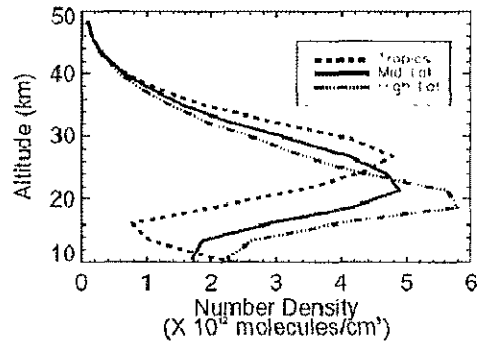
SAGE II O<sub>3</sub> Profiles September 1994

Figure 1: Typical ozone profiles from three different locations: Tropics, Mid-latitude, and High (polar) Latitude in the northern hemisphere.<sup>1</sup>

Ozone is considered one of the most essential components of the atmosphere because stratospheric ozone protects us from harmful, ultraviolet solar radiation. It is generally regarded that life on Earth could not begin until ozone existed. After being one of the first atmospheric compounds to be placed on the endangered list, ozone became the first chemical to be protected by international treaty.<sup>2</sup>

## 1.2 Stratospheric Ozone

Ozone is found naturally throughout the stratosphere, but is concentrated in the lower half of the stratosphere. Stratospheric ozone performs the

important job of protecting the Earth by absorbing the harmful ultraviolet radiation from the sun.

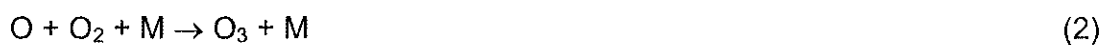
The stratosphere begins approximately 10 kilometers above the surface of the Earth to about 50 kilometers.<sup>2</sup> Approximately 10% of all atmospheric mass is found in the stratosphere.<sup>2</sup> This region of the atmosphere is very stable and is quite resistant against vertical motions (i.e. vertical mixing of particles and gases). The stable condition is due to a temperature inversion, which occurs as the stratosphere is heated from the absorption of ultraviolet radiation and the region it overlies becomes relatively cooler.<sup>3</sup> The temperature within this area remains constant and even increases with higher altitudes.<sup>2</sup>

### **1.2.1 Ozone Formation in the stratosphere**

Ozone is formed in the stratosphere when sunlight reacts with molecular oxygen in the upper atmosphere. Specifically, the photochemical reactions to produce ozone begin with photodissociation. The process of photodissociation takes place when ultraviolet radiation (UV) is absorbed by an O<sub>2</sub> molecule. The energy absorbed from the UV photon is sufficient to break the molecular bonds of the O<sub>2</sub> molecule. This process causes the molecular O<sub>2</sub> to separate or dissociate into atomic oxygen as shown in equation (1).



The atomic oxygen atoms produced from photodissociation quickly react with another molecular oxygen and a third body to form ozone in a reaction known as a three-body reaction as shown in equation (2).



The third body in a three-body reaction usually denoted by M does not actively participate in the reaction and is not chemically altered. It is added to complete the chemical equation by carrying away excess kinetic energy. In the atmosphere, nitrogen and oxygen are the most common third bodies because of their abundance.<sup>2</sup> The photochemical equations of (1) and (2) produce an overall net reaction. For every three molecular oxygen, two ozone molecules are produced.





Since molecular oxygen is uniformly distributed throughout the atmosphere, ozone is produced wherever UV radiation is incident to the atmosphere, generally at altitudes between 20 and 30 kilometers.<sup>2</sup> At this range of altitude, ozone is continuously produced. The photodissociation does not normally occur at altitudes lower than 20 km, which is the lower part of the stratosphere.<sup>2</sup> The reason for this is at higher altitudes most of the UV sunlight with wavelengths of less than 250 nanometers is absorbed by the O<sub>2</sub> and O<sub>3</sub> molecules. At altitudes higher than 30 km, ozone is constantly produced, but a counter reaction constantly destroys ozone, resulting in a steady-state concentration.

The constant production of ozone in the stratosphere provides the crucial layer which protects the atmosphere from the sun's harmful UV radiation. However, there is a competing photochemical reaction used to naturally maintain ozone levels in the stratosphere. Without the competing mechanism, most of the oxygen in the atmosphere would be converted to ozone. The photochemical reactions used to eliminate ozone occur in the same region as ozone production. Photo-dissociation also occurs with ozone. The UV photon absorbed by an ozone molecule will cause it to separate into atomic oxygen and molecular oxygen as shown in equation (4).



Note that the photo-dissociation of ozone occurs much faster than the photo-dissociation of  $O_2$ .<sup>2</sup> The atomic oxygen produced by the photo-dissociation of ozone will immediately react with  $O_2$  to regenerate ozone. Atomic oxygen can also react with ozone to produce two molecular oxygen molecules as illustrated in equation (5).



The net reaction of equations (4) and (5) produce three  $O_3$  molecules for every two  $O_2$  molecules.



Due to the relative concentrations of  $O_2$  and  $O_3$  in the atmosphere, atomic oxygen will have a higher probability (millions times more frequently) of reacting with an  $O_2$  molecule than an  $O_3$  molecule.<sup>2</sup>

### 1.2.2 Anthropogenic Destruction of Stratospheric Ozone

Unfortunately, certain chemical agents normally released into the atmosphere by human activity can also destroy ozone via a catalytic reaction. With catalytic reactions, a specific agent reacts with oxygen and the specific agent is regenerated through the process. This catalytic reaction can have an adverse effect on the ozone concentrations protecting the Earth and thereby negatively affect life on the planet. In the stratosphere, the following chemical compounds or catalysts are identified for ozone destruction: chlorine (Cl), nitric oxide (NO), bromine (Br), and hydroxyl (OH).<sup>2</sup> These catalysts are normally released into the atmosphere by human effects such as automobile emissions and spray aerosol cans. The following reactions illustrate the catalytic reaction cycle with X representing one of the listed catalysts.



Equation (7) illustrates the catalytic process and demonstrates how a catalyst (X) can destroy an ozone molecule and then regenerate itself. The net result is two molecular oxygen molecules formed from atomic oxygen and an ozone molecule.



Since the catalyst can be recycled, one catalyst molecule may possibly destroy tens of thousands of ozone molecules.<sup>4</sup> The catalyst will continue to destroy ozone molecules until another reaction converts it to a less aggressive compound. Therefore, potentially small amounts of catalytic compounds released in the air can deplete ozone concentrations in the atmosphere.

An example of a catastrophic consequence from the destruction of stratospheric ozone is illustrated in Figure 2. Over the region of Antarctica, ozone concentrations are substantially lower as compared to the rest of the planet and this region is referred as the "ozone hole." Reported findings show a decrease of as much as 95% in ozone above Antarctica.<sup>5</sup> Figure 2 shows measurements taken by the SAGE II satellite from a region over Antarctica (ozone hole) and the northern polar region (typical ozone profile) to compare the drastic difference. This illustrates a serious consequence of what can happen if the destruction of ozone goes unchecked.

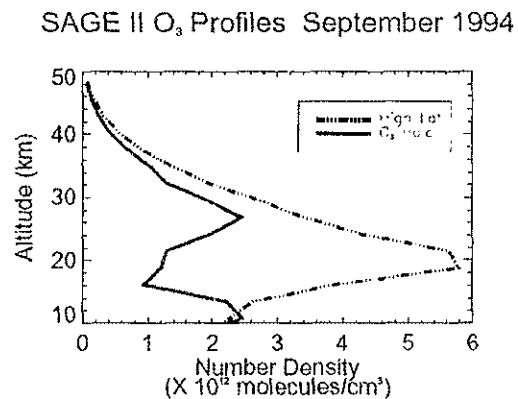


Figure 2: A comparison between a typical ozone profile and the ozone hole over Antarctica.<sup>1</sup>

### 1.3 Tropospheric Ozone

The troposphere is that part of the atmosphere from the surface of the Earth to approximately 10 km. Even though ozone protects the Earth, high, near-ground ozone concentrations are considered harmful and can cause many health problems. It is a secondary component of smog and predominately found in large urban cities. As more cities continue to grow and become more industrialized, the problem of smog and ozone increases.

The troposphere, the lowest region of the Earth's atmosphere, holds 90% of the atmosphere's total mass and the air within this region is typically unstable due to decreasing temperatures at higher altitudes.<sup>2</sup> The instability is

the result of the decreasing temperature, which causes convection or vertical motion of the troposphere. As sunlight heats the surface of the Earth, convection occurs and produces a buoyancy effect in the air. This vertical motion develops a mixing effect that can cause turbulence, which generally exhibits weather patterns. The effect is especially important to atmospheric dispersion and air pollution.<sup>2</sup>

### **1.3.1 Ozone Formation in the Troposphere**

In the troposphere, ozone is a component of smog and is a major concern for polluted cities. Tropospheric ozone is a result of harmful contaminants being released in the atmosphere. The primary source of the pollutants is from automobile emissions, which emit carbon monoxide (CO), nitrogen oxides (NO and NO<sub>2</sub>), and reactive hydrocarbons.<sup>6</sup> It is the combination of these chemical compounds and sunlight that produce ozone and numerous other pollutants.

Tropospheric ozone is a secondary pollutant and is not directly created from the chemical compounds released into the air, but formed from the result of nitrogen dioxide production. The nitric oxide (NO) released into the air reacts with a compound (RO<sub>2</sub>), which is produced from an organic radical represented by a general term R and molecular oxygen O<sub>2</sub>. This reaction produces nitrogen dioxide (NO<sub>2</sub>) as shown in equation (9).



Organic radicals are composed of many atoms with a complex molecular structure and it is not necessary to identify a specific radical.<sup>2</sup> The production of organic radicals, which originates from the reactions of hydroxyl radicals and harmful reactive hydrocarbons, is a part of a more complex atmospheric process.<sup>2</sup> Only the relevant equations for the production of ozone are discussed in this thesis. Photo-dissociation occurs with nitrogen dioxide to produce small amounts of NO and O that are released into the air, as shown in equation (10).



The atomic oxygen produced reacts with molecular oxygen to produce ozone, as illustrated in equation (11).



The competing reaction to eliminate ozone results from the NO produced is in equation (10). The nitric oxide can then react with ozone to produce NO<sub>2</sub> and O<sub>2</sub>, as shown in equation (12).



The previous three sequences of equations establishes the steady state of concentrations for NO, NO<sub>2</sub>, and O<sub>3</sub>.

### 1.3.2 Ozone as a Harmful Pollutant

A variety of health problems can arise from the exposure to ozone. Ozone can easily be sensed through the nose and is often characterized by a sweet aroma. Being exposed to low concentrations of ozone, about 0.1 part per million volume (ppmv), can irritate the respiratory tract.<sup>2</sup> People who are sensitive are more likely to be affected, especially the elderly and young children. Higher concentrations of ozone, such as concentrations of about 1 ppmv, may cause breathing difficulties and headaches. Ozone oxidizes human tissue, and long-term exposure, even at low concentrations, may damage sensitive skin areas and prematurely age lung tissue.<sup>7</sup> The oxidation process



is similar to receiving a very slow burn. As ozone concentrations increase, so too do the oxidation rate and the physiological effects.

#### **1.4 Atmospheric Measurements**

Climate and air quality have become increasingly important due to environmental and health issues. As a result, there are increasing demands for fundamental atmospheric measurements and mounting needs for monitoring the ozone hole, overall stratospheric level and the tropospheric ozone.

Two general approaches are used for atmospheric measurements. The first approach involves using such instruments as rocketsondes and balloonsondes for direct sampling (in-situ) of the atmosphere in which atmospheric samples are analyzed directly for its properties and relative amounts of various chemical components. In-situ measurements have the advantage of good resolution over localized regions but cannot offer a global picture of ozone distribution.<sup>1</sup> The second approach involves remote sensing, through which radiation in the form of electromagnetic waves is used to interact and obtain various information, such as measurements, about ozone and other atmospheric elements. The information is obtained without placing the sensor in direct contact with the atmospheric samples. Remote sensing allows the

advantage of reaching difficult or inaccessible areas, and, in comparison, can be fast and inexpensive in measuring large volumes.

Two types of remote sensing approaches are used for atmospheric investigations. The first, known as passive remote sensing, does not emit any radiation but uses naturally occurring radiation such as sunlight to obtain information about ozone and other atmospheric species. A disadvantage of passive remote sensing is that it cannot provide high-resolution vertical distributions of ozone.<sup>8</sup> The second type of approach, active remote sensing produces and emits radiation in the form of light, radio waves, microwaves, or acoustic waves. The radiation is backscattered by the atmosphere and analyzed. Active remote sensing has the advantage of being independent of natural radiation sources and the time of day, and also has the ability to control the stimulating signal.<sup>7</sup> Radar and lidar are some examples of active remote sensing systems. Lidar has a primary advantage of providing high vertical resolution profiles at various altitudes and has been deployed on various platforms.<sup>9</sup>

Ozone profiles from various instruments are shown in figure 3. The instruments demonstrate the two general approaches used for atmospheric measurements. The comparisons shown in figure 3 show reasonable agreement between, lidar, satellite (SAGE II), rocketsondes (ROCOZ-A), and balloonsondes (ECC).

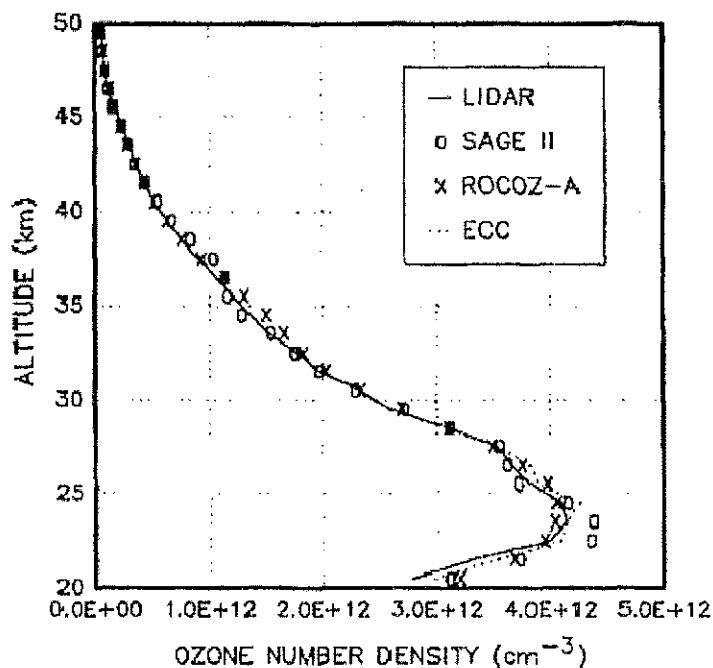


Figure 3: Ozone profiles from various instruments.<sup>5</sup>

A variety of platforms such as balloons, aircraft, satellites and ground-based systems have been used to conduct atmospheric measurements.<sup>1</sup> Employing a variety of platforms allows the ability to validate and complement various measurements by different platforms.<sup>1</sup> For many years, balloons and ground-based platforms provided accurate ozone profiles (vertical distributions) but lacked the ability to map ozone profiles over a worldwide scale.<sup>1</sup> Aircraft platforms can provide ozone profiles over various regions in the atmosphere and have been used to validate satellite measurements.<sup>10</sup> Satellite platforms



## 1.5 Research Objective

In the previous sections, the significance of ozone, its role in protecting the planet and its role as a pollutant have been discussed. More information is needed to increase our knowledge and understanding of the global impact of ozone and its impact on mankind. As a result, there is an increasing need for ozone atmospheric measurements. This thesis describes research on a compact ozone lidar, which is capable of measuring both ozone and aerosols. The purpose of this research thesis is to study and characterize the operation of this ozone lidar system. This system will eventually be deployed for aircraft-based, and possibly unpiloted atmospheric vehicle (UAV), ozone and aerosol measurements to improve our understanding of ozone production and transport.

## CHAPTER II

### LIDAR CONCEPTS AND THEORY

This chapter covers basic lidar system architecture along with the theory of the lidar equation and the related differential absorption lidar equation. In addition, the concept of frequency conversion will be discussed because it is a critical piece for obtaining the ultraviolet wavelength needed for the lidar system.

#### 2.1 Lidar System Architecture

The term lidar is an acronym, which stands for light detection and ranging. The lidar concept mimics the techniques of radar but uses optical wavelengths instead of radio signals. A basic lidar system in principle consists of a transmitter and a receiver, a data acquisition and control subsystem and a computer for data analysis. A block diagram of a typical lidar system is shown in figure 5.

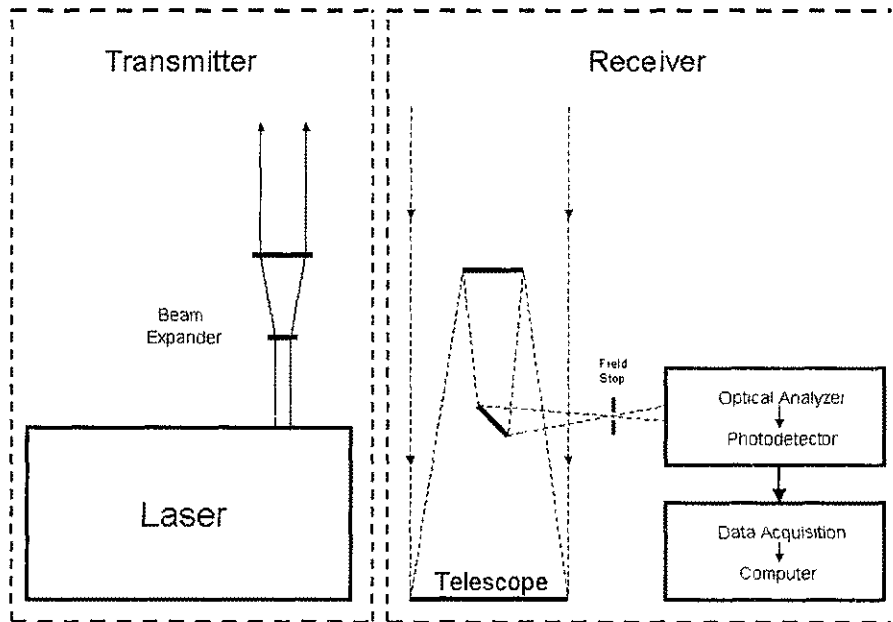


Figure 5: A conceptual illustration of a lidar system showing major components.

A transmitter is used to send a short-pulse laser beam toward a specific region in the atmosphere. Prior to being transmitted into the atmosphere, lidar systems often employ a beam expander within the transmitter to decrease divergence of the laser beam. In the atmosphere, the laser light interacts with atmospheric aerosols (suspended particles in the air) or air molecules, which causes some of the laser light to scatter back towards a receiver. The backscattered light contains only a small portion of energy from the emitted

laser pulse. The receiver system contains a telescope to collect the backscattered light, which focuses the collected light onto an optical analyzing system that filters specific wavelengths or polarization states out of the collected light. The filtered light is directed onto a photodetector within the receiver system and converts the backscattered light into an electrical signal. Using an analog to digital converter, the electrical signal is digitized and stored then analyzed by a computer. During the analysis, the concentration of atmospheric molecules like ozone can be determined as a function of range or distance.

Lidar systems are arranged in two basic configurations. The first is the bi-static configuration, which entails separating the transmitter and receiver by a certain distance to achieve spatial resolution. The second and most common design is the mono-static configuration in which the transmitter and receiver are in the same location and is setup in either a co-axial or bi-axial arrangement. In co-axial setups, the laser beam axis is coincident with the axis of the receiver optics and this allows the laser beam to be in constant view of the telescope. In bi-axial arrangements, the laser beam axis and the axis of the receiver are separated in a way that after a pre-determined distance the laser beam enters the telescope's field of view. This arrangement avoids saturation of the photodetector by near-field atmospheric backscatter return signal.<sup>12</sup>



## 2.2 Lidar Equation

The general lidar equation is the fundamental equation used to predict the number of photons backscattered to the receiver from a given distance. The development of the general lidar equation begins with two assumptions made about the atmospheric scattering process.<sup>12</sup> The first assumption implies that all atmospheric constituents have random motion and are adequately separated, as such, there is no phase relation so that the total scattered energy is the sum of energy scattered from each atmospheric particle. The second assumption assumes only single scattering occurs, whereas a laser photon is scattered only once before being captured by the telescope.

In the atmosphere, scattered light can be categorized into two general groups.<sup>12</sup> The first group is elastic scattering in which the scattered light has the same wavelength as the transmitted laser light. Rayleigh and Mie scattering are typical examples of elastic scattering and are dependent on the size of the atmospheric molecule compared to the laser wavelength. In the second group, inelastic scattering, the wavelength of the scattering light is shifted due to the excitation of the energy levels of the scattering molecule. Raman scattering is a classical example of inelastic scattering. Only elastic scattering is considered in this thesis. To show how the lidar equation was derived, figure 6 illustrates a physical picture of the lidar equation with a block diagram of a lidar system.

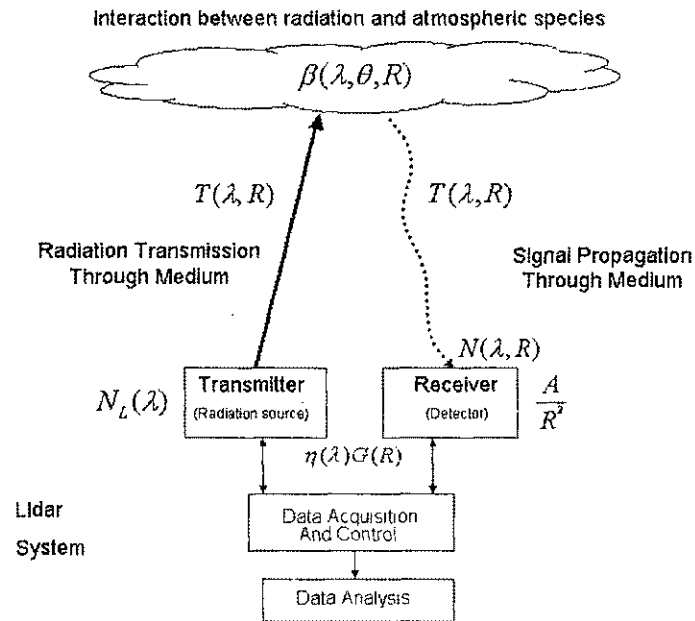


Figure 6: A physical picture of the lidar equation.

The elastic form of the lidar equation is given as<sup>12</sup>

$$N(\lambda, R) = N_L(\lambda) \beta(\lambda, \theta, R) \frac{c\tau}{2} \frac{A}{R^2} \eta(\lambda) G(R) T^2(\lambda, R) \quad (13)$$

where

$N(\lambda, R)$       Number of photons received in the telescope's field of view

$N_L(\lambda)$	Number of photons transmitted by the laser
$\beta(\lambda, \theta, R)$	Backscattered coefficient of the target atmospheric species
$\frac{c\tau}{2}$	Effective spatial pulse length
$\frac{A}{R^2}$	Probability that a backscattered photon is collected by the telescope where A is the area of the telescope and R is the range
$\eta(\lambda)$	Overall receiver's optical efficiency
$G(R)$	Overlap geometric factor of the laser beam and Receiver's field of view
$T^2(\lambda, R)$	Transmission of emitted laser light (photons) through the atmosphere and back to the telescope

A geometric illustration of the lidar equation is shown in figure 7 and will aid in the discussion of the lidar equation.

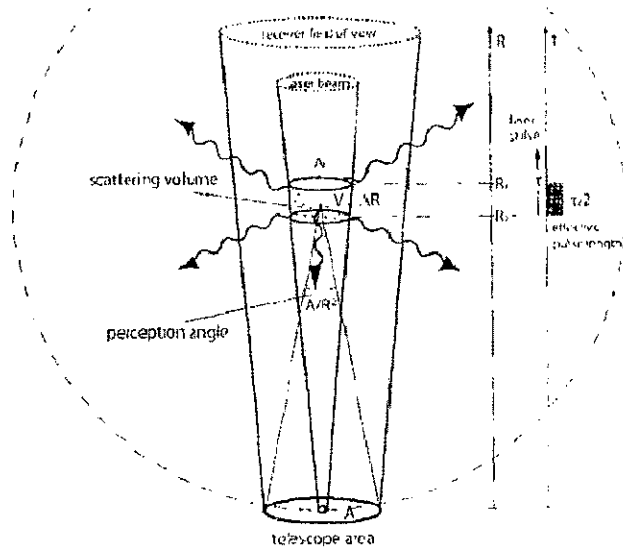


Figure 7: An illustration of the lidar equation.<sup>13</sup>

The terms  $N(\lambda, R)$  and  $N_L(\lambda)$  represent the number of photons received by the telescope and the number of photons transmitted by the laser transmitter, respectively. The number of photons  $N$  is determined by the power of the laser pulse  $P$  multiplied by the integration time  $\Delta t$  and laser wavelength  $\lambda$  divided by Planck's constant  $h$  and the speed of light  $c$ .

$$N = \frac{P\Delta t\lambda}{hc} \quad (14)$$

The primary atmospheric factor that determines the strength of the lidar return signal is the backscatter coefficient  $\beta(\lambda, \theta, R)$ , which describes the amount of light scattered back towards the lidar receiver from a given distance.<sup>13</sup> The value for the scattering coefficient is specific to the scattering angle, which is usually  $180^\circ$  for lidar applications. In the atmosphere, laser light is scattered by aerosols (particulate matter) and air molecules.<sup>14</sup> Aerosol scattering is highly erratic on all temporal and spatial scales in the atmosphere.<sup>13</sup> However, molecular scattering largely depends on air density and will decrease with altitude.<sup>13</sup> The backscatter coefficient can be written as a summation of all backscatters as

$$\beta(\lambda, \theta, R) = \sum_j N_j(R) \frac{d\sigma_{j,scatter}}{d\Omega}(\lambda, \theta) \quad (15)$$

The term  $d\sigma_{j,scatter}(\lambda, \theta)/d\Omega$  represents the differential scattering cross section of the particle at the scattering angle  $\theta$  and wavelength  $\lambda$ . The term  $N_j(R)$  represents the concentrations of scattering particles of species  $j$  in the volume illuminated by the laser pulse.

The illuminated scattering volume is determined by calculating the range  $R$ . A return lidar signal is detected at time  $t$  after the leading edge of the laser

pulse is transmitted. The backscattered light from the leading edge of the laser pulse traveled the distance  $R_1 = ct/2$ , where  $c$  is the speed of light. During the same period, the trailing edge of the transmitted pulse is detected from distance  $R_2 = c(t - \tau)/2$ , where  $\tau$  is the temporal laser pulse length. Therefore, the length of the volume from the backscattered light received at time instant  $t$  is  $\Delta R = R_2 - R_1 = c\tau/2$  which is called the effective spatial pulse length or the range resolution of the lidar signal.<sup>13</sup> Together, the product of the backscatter coefficient  $\beta$  and  $\Delta R$  determines the angular scattering probability.

The term  $A/R^2$  represents the capture angle or the probability a backscattered photon is gathered by the receiving telescope, where  $A$  is the area of the telescope and  $R$  is the distance the backscattered photon traveled.<sup>15</sup>

The term  $\eta$  represents the optical efficiency of the lidar receiver system hardware (e.g. receiver mirrors, lens, filters, and detectors) and  $G(R)$  is the geometric factor that characterizes the area of overlap of the laser beam with the receiver field of view. Once there is complete overlap this factor is one.

The term  $T^2(\lambda, R)$ , which is the transmission of the emitted laser pulse and the return signal through the atmosphere, describes the amount of light that is lost on the way to and from the atmospheric scattering volume.<sup>14</sup> The transmission term is a specific form of the Lambert-Beer-Bouguer equation derived for lidar and is given by<sup>13</sup>

$$T^2(\lambda, R) = \exp\left[-2 \int_0^R \alpha(R, \lambda) dr\right] \quad (16)$$

where  $\alpha$  is the extinction coefficient. The extinction coefficient represents the sum of all transmission losses and is given by

$$\alpha(R, \lambda) = \sum_j N_j(R) \sigma_{j,ext}(\lambda) \quad (17)$$

where  $N_j$  represents the concentrations of scattering type  $j$  and  $\sigma_{j,ext}(\lambda)$  is the extinction cross-section for each type of scatter  $j$ . Given that extinction may occur because of the scattering and absorption of light by particles and molecules, the extinction coefficient can be written as the total of four components,<sup>13</sup>

$$\alpha_{total}(R, \lambda) = \alpha_{mol,scat}(R, \lambda) + \alpha_{mol,abs}(R, \lambda) + \alpha_{aero,scat}(R, \lambda) + \alpha_{aero,abs}(R, \lambda) \quad (18)$$

where  $\alpha_{mol,scat}$  is the extinction from molecular scattering,  $\alpha_{mol,abs}$  is the extinction from molecular absorption,  $\alpha_{aero,scat}$  is the extinction from aerosol

scattering, and  $\alpha_{aero,abs}$  is the extinction from aerosol absorption. The four extinction components are a function of range and wavelength. The total extinction cross-section  $\sigma_{extinction}(\lambda)$  is the sum of the scattering (integrated) cross-section and the absorption cross-section,<sup>16</sup>

$$\sigma_{extinction}(\lambda) = \sigma_{scat}(\lambda) + \sigma_{abs}(\lambda) \quad (19)$$

where  $\sigma_{scat}(\lambda)$  is the total scattering cross-section integrated in all directions and  $\sigma_{abs}$  is the absorption cross-section.

A more general form of the lidar equation is normally utilized by using the power transmitted  $P_0$  instead of the number of photons transmitted  $N_L$  to allow a lidar return signal in units of watts. The more general form of the lidar equation is shown in equation (20).

$$P(R) = P_0 \beta(\lambda, \theta, R) \frac{c\tau}{2} \frac{A}{R^2} \eta(\lambda) G(R) T^2(\lambda, R) \quad (20)$$



### 2.3 DIAL Equation

Differential absorption lidar (DIAL) is a specialized technique used in remote sensing of ozone profiles in the atmosphere.<sup>17</sup> The technique transmits two laser wavelengths in the UV spectrum to measure the difference in the atmospheric absorption by ozone between the two lidar wavelengths. One wavelength is chosen with strong ozone absorption and is identified as the on-line wavelength ( $\lambda_{on}$ ). The other wavelength known as the off-line wavelength ( $\lambda_{off}$ ) has lower ozone absorption. By analyzing the power of the lidar return signal for both wavelengths, the average ozone concentration over a selected range interval is determined. The absorption cross-section of ozone with the two wavelengths used in this ozone lidar (vertical lines) is shown in figure 8. The graph shows a specific range of wavelengths where the absorption cross-section of ozone decreases as wavelength increases. Additionally, the graph shows the absorption cross-section difference between typical on-line (290-nm) and off-line (300-nm) wavelengths. Typically the on-line and off-line laser beams are transmitted with a time separation of  $\sim 300 \mu s$  to make certain the same atmospheric scattering volume is measured by both wavelengths.<sup>18</sup>

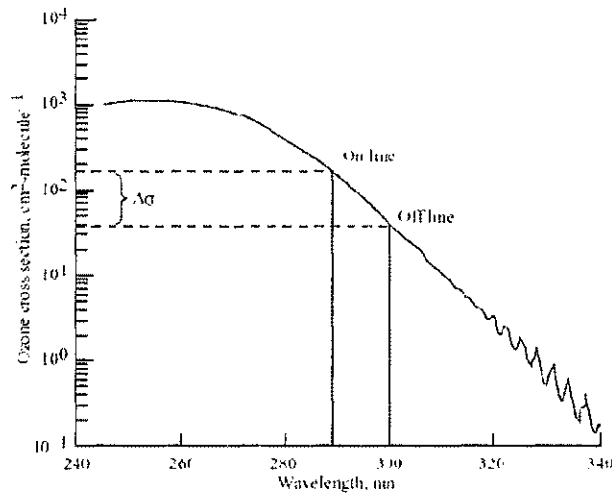


Figure 8: Absorption cross-sections of ozone in the UV spectrum with the wavelengths used in the lidar of this thesis (vertical lines).<sup>19</sup>

The derivation of the DIAL equation begins with the ratio of the received lidar signals from both on-line and off-line wavelengths. Using equation (20) for elastic scattering and taking the ratio of the  $P(\lambda_{on}, R)$  to  $P(\lambda_{off}, R)$  the DIAL equation is given as

$$\frac{P(\lambda_{on}, R)}{P(\lambda_{off}, R)} = \frac{P_L(\lambda_{on})\beta(\lambda_{on}, R)\Delta R \frac{A}{R^2} \eta(\lambda_{on})G(R)T^2(\lambda_{on}, R)}{P_L(\lambda_{off})\beta(\lambda_{off}, R)\Delta R \frac{A}{R^2} \eta(\lambda_{off})G(R)T^2(\lambda_{off}, R)} \quad (21)$$

where  $P(\lambda_{on}, R)$  is defined as the lidar return signal at wavelength  $\lambda_{on}$  and  $P(\lambda_{off}, R)$  at wavelength  $\lambda_{off}$ . The system function  $\eta(\lambda)G(R)$  and output laser power  $P_L(\lambda)$  for  $\lambda_{on}$  and  $\lambda_{off}$  wavelengths cancel out based on the assumption of being equal thus leaving a ratio of backscatter and transmission extinction terms.

$$\frac{P(\lambda_{on}, R)}{P(\lambda_{off}, R)} = \frac{\beta(\lambda_{on}, R)T^2(\lambda_{on}, R)}{\beta(\lambda_{off}, R)T^2(\lambda_{off}, R)} \quad (22)$$

The atmospheric transmission terms can be written as

$$\frac{T^2(\lambda_{on}, R)}{T^2(\lambda_{off}, R)} = \exp\{-2 \int_0^R [\alpha(\lambda_{on}, R) - \alpha(\lambda_{off}, R)] dR\} \quad (23)$$

where  $\alpha(\lambda_{on,off}, R)$  are the total atmospheric extinction coefficients for the on-line and off-line wavelengths. Thus substituting equation (23) into equation (22) gives

$$\frac{P(\lambda_{on}, R)}{P(\lambda_{off}, R)} = \frac{\beta(\lambda_{on}, R)}{\beta(\lambda_{off}, R)} \exp\left\{-2 \int_0^R [\alpha(\lambda_{on}, R) - \alpha(\lambda_{off}, R)] dR\right\} \quad (24)$$

In order to obtain the ozone number density from the extinction coefficient, the backscatter ratio term is shifted to the left side and taking the natural logarithm of both sides

$$\ln \left[ \frac{P(\lambda_{on}, R) \beta(\lambda_{off}, R)}{P(\lambda_{off}, R) \beta(\lambda_{on}, R)} \right] = -2 \int_0^R [\alpha(\lambda_{on}, R) - \alpha(\lambda_{off}, R)] dR \quad (25)$$

The total extinction coefficient can be decomposed into

$$\alpha(\lambda, R) = \alpha'(\lambda, R) + N(R)\sigma(\lambda) \quad (26)$$

where  $\alpha'(\lambda, R)$  is the extinction coefficient specific for ozone absorption,  $N(R)$  is the molecule number density of ozone at range  $R$ , and  $\sigma(\lambda)$  is the absorption cross-section at wavelength  $\lambda$ . After substituting equation (26) into equation (25) and taking the derivative the result is

$$\frac{d}{dR} \ln \left[ \frac{P(\lambda_{on}, R) \beta(\lambda_{off}, R)}{P(\lambda_{off}, R) \beta(\lambda_{on}, R)} \right] = -2 \left\{ [\alpha'(\lambda_{on}, R) + N(R) \sigma(\lambda_{on})] \right. \\ \left. - [\alpha'(\lambda_{off}, R) + N(R) \sigma(\lambda_{off})] \right\} \quad (27)$$

Solving for the molecule number density of ozone  $N(R)$  results in

$$N(R) = \frac{1}{2[\sigma(\lambda_{on}) - \sigma(\lambda_{off})]} \frac{d}{dR} \ln \left[ \frac{P(\lambda_{on}, R) \beta(\lambda_{off}, R)}{P(\lambda_{off}, R) \beta(\lambda_{on}, R)} \right] - \frac{\alpha'(\lambda_{on}, R) - \alpha'(\lambda_{off}, R)}{[\sigma(\lambda_{on}) - \sigma(\lambda_{off})]} \quad (28)$$

where  $\sigma(\lambda_{on}) - \sigma(\lambda_{off}) = \Delta\sigma$  is the difference between the ozone absorption cross-section at the on-line and off-line wavelengths. If the difference between the on-line and off-line wavelengths is small, the extinction coefficients are assumed to be essentially the same and thus can be canceled out.<sup>11</sup> The extinction terms  $\alpha'(\lambda_{on}, R) - \alpha'(\lambda_{off}, R) = 0$  and equation (28) becomes

$$N(R) = \frac{1}{2[\Delta\sigma]} \frac{d}{dR} \ln \left[ \frac{P(\lambda_{on}, R) \beta(\lambda_{off}, R)}{P(\lambda_{off}, R) \beta(\lambda_{on}, R)} \right] \quad (29)$$

Based on the assumption that the difference between the on-line and off-line wavelengths is small, the backscattering coefficients for both wavelengths are in essence the same.<sup>11</sup> After canceling the backscattering coefficients, equation (29) can now be simplified to be

$$N(R) = \frac{1}{2[\Delta\sigma]} \frac{d}{dR} \ln \left[ \frac{P(\lambda_{on}, R)}{P(\lambda_{off}, R)} \right] \quad (30)$$

In addition, assuming the number density function is constant over a small interval, the interval is defined as the range cell  $\Delta R = (R_2 - R_1)$ . The final DIAL equation becomes

$$N(R) = \frac{1}{2\Delta\sigma\Delta R} \ln \left[ \frac{P(\lambda_{on}, R_1)P(\lambda_{off}, R_2)}{P(\lambda_{off}, R_1)P(\lambda_{on}, R_2)} \right] \quad (31)$$

This form of the DIAL equation provides a method of calculating atmospheric ozone concentration as a function of range. The concentration of ozone is determined by the natural logarithm of the received powers for the on-line and off-line wavelengths for a given range cell  $\Delta R = (R_2 - R_1)$ . The smaller the

range cell, the more accurate the DIAL equation becomes. Also note the equation is not dependant on the transmitted pulse power  $P$  so long as a return laser signal is received for the given range.

## 2.4 Frequency Conversion

Many of the available laser sources are limited in wavelength range and offer only fixed wavelengths. For example the neodymium ( $\text{Nd}^{3+}$ ) lasers (e.g. Nd:YAG, Nd:YLF) produce laser light in the infrared region and have found important uses in scientific, medical, military, and industrial applications. However, the remote sensing of ozone requires laser light to be transmitted in the UV region as shown in figure 8. A method is required to produce UV laser light from high-powered infrared laser sources.

The use of frequency conversion is a valuable technique for expanding the utility of high-powered lasers.<sup>20</sup> The technique generates new frequencies (wavelengths) by utilizing the nonlinear optical response of a specific optical crystal by intense laser radiation fields.<sup>21</sup> Generally, only laser light has the intensity to modify the optical properties of an optical medium. Frequency conversion includes harmonic generation used to double, triple, and quadruple the fundamental frequencies of laser sources.<sup>21</sup> Frequency doubling and quadrupling crystals are currently used to generate second harmonic and fourth

harmonic wavelengths in neodymium laser sources to produce laser light in the UV region for ozone measurements.<sup>22</sup> The first example of second harmonic generation was demonstrated in 1961 with the use of a ruby laser with a wavelength of 694.3 nm. The ruby laser incident on a quartz crystal generated laser light exactly one-half the wavelength of the ruby laser.<sup>22</sup>

Physically, second harmonic generation can also be viewed as the exchange of photons between a range of frequency components of the electric field. In a single quantum process, two photons of frequency  $\omega$  are destroyed and a photon of frequency  $2\omega$  is simultaneously created.<sup>24</sup> Figure 9 illustrates this process where the horizontal solid line represents the atomic ground state and the dashed lines represent the virtual levels of the nonlinear crystal. The virtual levels symbolize the combined energy of one of the energy eigenstates of the atom along with one or more photons of the radiation field.<sup>24</sup>

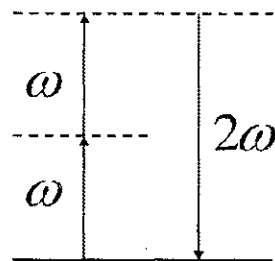


Figure 9: Energy-level diagram illustrating second harmonic generation.



The optical nonlinearity response of a crystal (Lithium Triborate -  $\text{LiB}_3\text{O}_5$  – a crystal used in this system) is described by the process of polarization or the dipole moment per unit volume  $\bar{P}(t)$  and is dependent on the strength of the applied optical field  $\bar{E}(t)$ . When an electric field enters an optical medium, it induces a polarization within the crystal. As the electromagnetic wave propagates through the crystal, changes occur in the distribution of electrical charges as the atoms and electrons respond to the wave's electromagnetic fields. The result is a displacement of the valence electrons, which create electric dipoles or induce polarization.<sup>21</sup> For weak field strengths, the polarization is proportional to the electric field (linear polarization), however, with higher field strengths, a nonlinear phenomena occurs with the re-radiation of the wave from dipoles whose amplitudes are distorted from the original sinusoidal electric field that generated the dipoles.<sup>21</sup> As a result, different frequencies are contained in the re-radiated wave.

In nonlinear optics, the nonlinear response or polarization  $\bar{P}(t)$  can be described as a power series in the field strength  $\bar{E}(t)$  as

$$\bar{P}(t) = \chi^{(1)}\bar{E} + \chi^{(2)}\bar{E}^2 + \chi^{(3)}\bar{E}^3 + \dots \quad (32)$$

where the constant of proportionality  $\chi^{(1)}$  is known as the linear susceptibility and is responsible for conventional linear optical effects and the quantities  $\chi^{(2)}$  and  $\chi^{(3)}$  are known as the second- and third-order nonlinear susceptibilities, respectively. Higher orders of susceptibility are small and thus require very high electric fields for the nonlinear optical effects to take place. To illustrate an example of nonlinear optical interaction, the laser beam for the process of second harmonic generation whose electric field strength is represented by

$$\bar{E}(t) = E \exp(i\omega t) + c.c. \quad \text{c.c.} = \text{complex conjugate} \quad (33)$$

is incident upon a crystal and gives rise to the nonlinear polarization for which the second-order susceptibility  $\chi^{(2)}$  is nonzero. The induced second-order nonlinear polarization created in the crystal is given by  $\bar{P}^{(2)}(t) = \chi^{(2)} \bar{E}^2(t)$  or as

$$\bar{P}^{(2)}(t) = 2\chi^{(2)} E E^* + (\bar{E}^2 \exp(-2\omega t) + c.c) \quad (34)$$

where the first term consists of a contribution at zero frequency which does not lead to the generation of electromagnetic radiation. The second term consists

of a contribution at frequency  $2\omega$  that leads to the generation of radiation at the second harmonic frequency.

### 2.4.1 Harmonic Generation

The creation of harmonic generation in a crystal by an incident wave of frequency  $\omega_1$  is viewed as a two-stage process. The first stage is the production of a polarization wave at the second harmonic  $2\omega_1$  that has a wavelength  $\lambda_p$  in the crystal that is determined by the index of refraction  $n_1$  of the incident wave and is expressed as

$$\lambda_p = \frac{c}{2\nu_1} n_1 \quad (35)$$

where  $c$  is the speed of light. The second stage is the transfer of energy from the polarization wave to an electromagnetic wave at frequency  $2\nu_1$ . For this electromagnetic wave, the wavelength  $\lambda_2$  is determined by the index of refraction  $n_2$  for the second harmonic wave, specifically,

$$\lambda_2 = \frac{c}{2\nu_1} n_2 \quad (36)$$

In order for efficient transfer of energy, it is essential that the polarization wave and the electromagnetic wave remain in phase. This implies the indexes of refraction are equal  $n_1 = n_2$ . In reality, crystals exhibit normal dispersion in the optical region and the radiation will usually lag behind the polarization wave.<sup>25</sup> This phase mismatch  $\Delta k$  between the polarization wave and the electromagnetic wave can be expressed as the difference in the wave number<sup>21</sup>

$$\Delta k = \frac{4\pi}{\lambda_1} (n_1 - n_2) \quad (37)$$

Using Maxwell's equations as a solution for a coupled incident wave and second harmonic wave propagating in the crystal, the generational efficiency of the second harmonic power can be determined from the ratio of powers between second harmonic frequency and incident frequency.<sup>21</sup> The second harmonic conversion efficiency may be approximated by<sup>25</sup>

$$\eta = \frac{P_{2\omega}}{P_{\omega}} = l^2 K \frac{P_{\omega}}{A} \frac{\sin^2(\Delta k l / 2)}{(\Delta k l / 2)^2} = l^2 K \frac{P_{\omega}}{A} \text{sinc}^2\left(\frac{\Delta k l}{2}\right) \quad (38)$$

where

$P_{2\omega}$	Power generated at second harmonic wavelength
$P_{\omega}$	Input power incident on the crystal
$l$	Length of nonlinear crystal
$K$	Nonlinear coefficient for a given crystal
$A$	Area of the input beam in the crystal
$\Delta k$	Phase mismatch between the polarization wave and electromagnetic wave

The conversion efficiency depends on the length of the crystal, the power density, and the phase mismatch. Typical second harmonic conversion efficiencies are approximately 50% for the lidar system used for this thesis. The term  $K$  is constant for a given crystal and wavelength. The second harmonic power generation, for a given crystal length, is strongly dependent on the phase mismatch as expressed in the  $\text{sinc}^2$  function. This function characterizes the

effect of the wave mismatch on the conversion efficiency. The second harmonic power is maximum when  $\Delta k = 0$  as seen in figure 10.

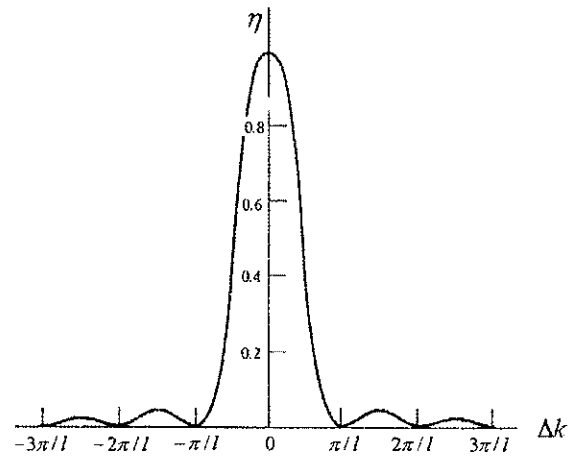


Figure 10: Second harmonic conversion efficiency as a function of the phase mismatch.

For a particular  $\Delta k$ , the second harmonic power grows and decays as a function of length  $l$  along the crystal with a period of  $\pi = \Delta k l / 2$ . The distance known as the coherence length  $l_c$  is half the period, which is the length from the crystal's entrance-face to the point the second harmonic power is at its maximum.<sup>26</sup> If the length of the crystal is less than  $l_c$  the second harmonic output increases quadratically, however if length of the crystal is greater than  $l_c$  the output will saturate and possibly decrease as  $l$  increases.<sup>26</sup>

A simple block diagram illustrating the basic principle of second and fourth harmonic generation used in the laser of this thesis is shown in figure 11.

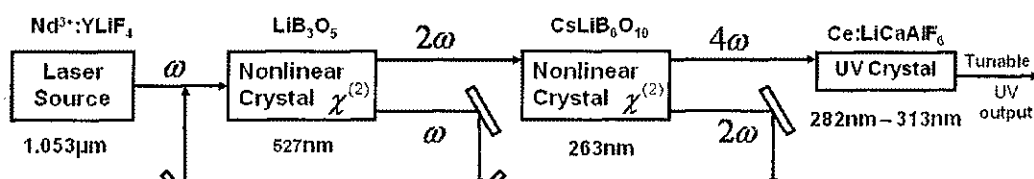


Figure 11: Block diagram showing the principle of second and fourth harmonic generation used in the laser of this thesis.

The fundamental wavelength  $1.053 \mu\text{m}$  produced by the  $\text{Nd}^{3+}:\text{YLiF}_4$  laser is incident on the first nonlinear crystal ( $\text{LiB}_3\text{O}_5$ ). Within the crystal, the fundamental frequency is doubled to produce the second harmonic wavelength 527-nm. This second harmonic wavelength is incident on the second nonlinear crystal ( $\text{CsLiB}_6\text{O}_{10}$ ) and again frequency doubled to produce the fourth harmonic wavelength of 263-nm. The fourth harmonic wavelength is used as a laser pump source to produce UV DIAL tunable wavelengths by the  $\text{Ce}:\text{LiCaAlF}_6$  UV crystal. These wavelengths are transmitted into the atmosphere to be used for DIAL ozone measurements.

## CHAPTER III

### EXPERIMENTAL SETUP

This chapter describes the hardware configuration of the ozone lidar system as shown in figure 12. The lidar system consists of several components with a complete schematic shown in figure 13. These components are divided into four primary subsystems: laser transmitter, receiver system, lidar control and support, and data acquisition. Each of the subsystems will be discussed in detail.

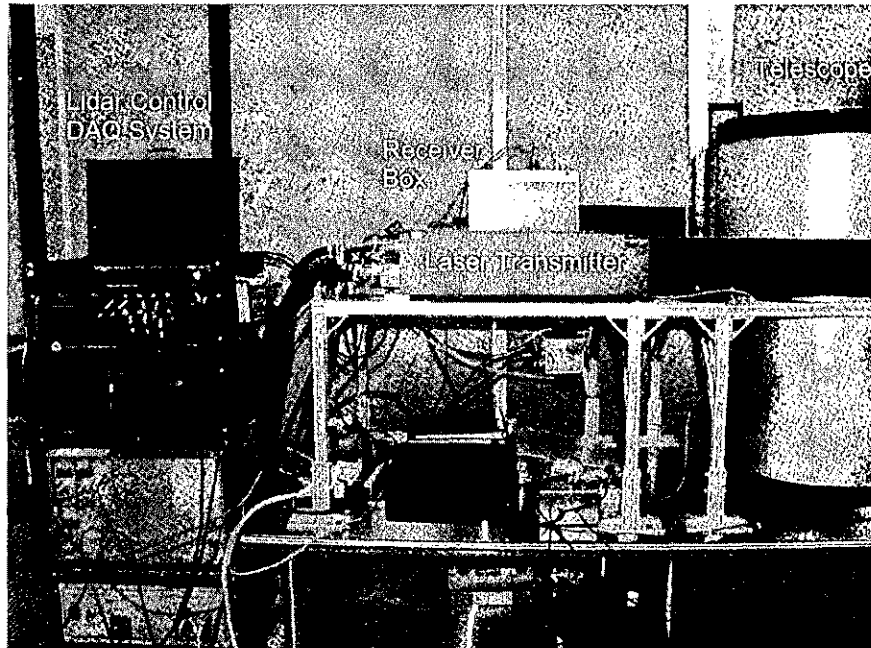


Figure 12: A picture of the ozone lidar system in the lab with the major components labeled.



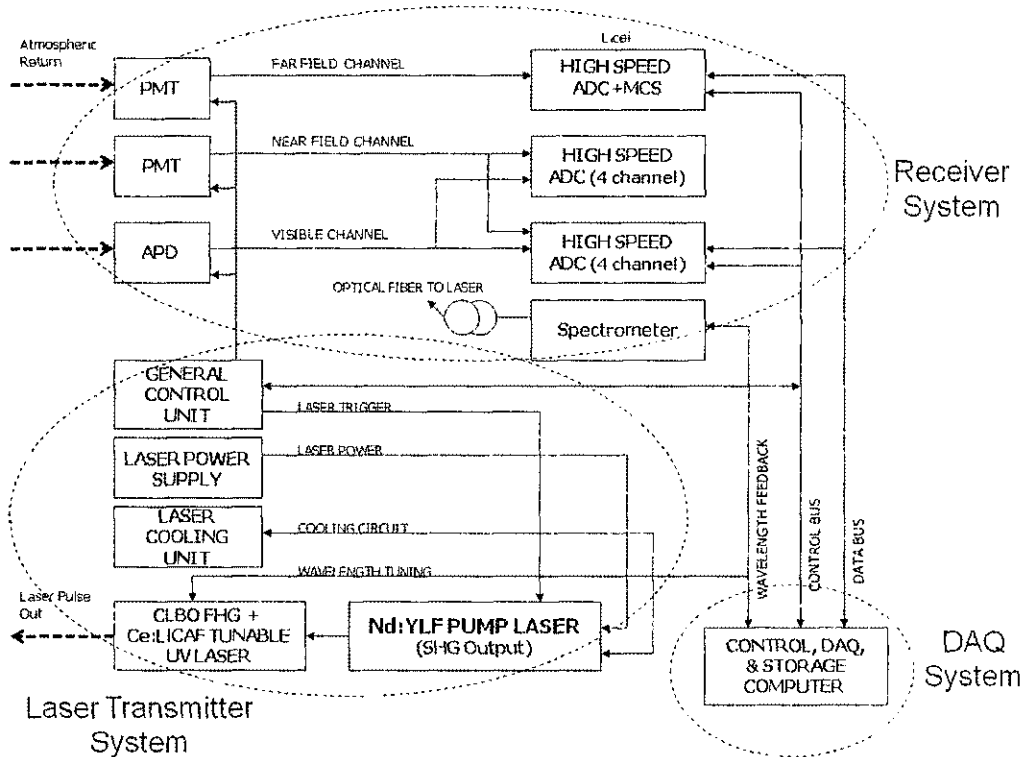


Figure 13: A schematic of the lidar system.

### 3.1 Lidar Transmitter

In this section, the main components of the laser transmitter system and its support units are discussed. The laser transmitter consists of a diode pumped Q-switched Nd:YLF pump laser and Ce:LiCAF tunable UV laser head with all the associated power and lidar control support units on a system rack. An optical schematic of the laser transmitter is shown in figure 14.

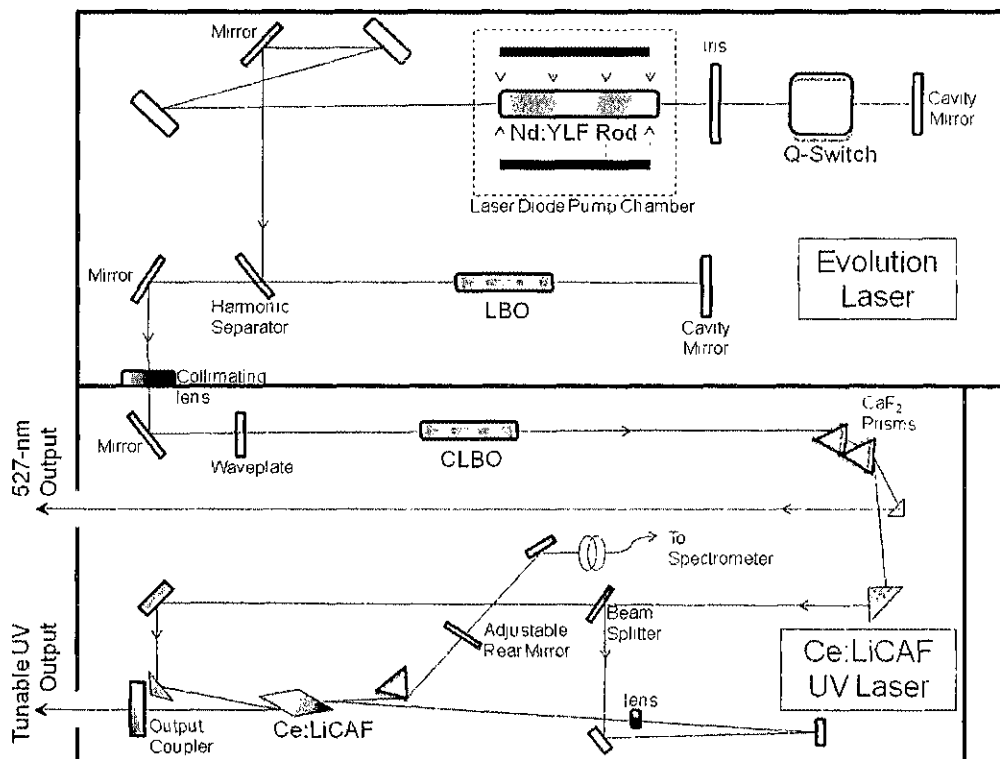


Figure 14: An optical schematic of the laser transmitter module which includes a Nd:YLF laser pump and a Ce:LiCAF tunable UV laser.

### 3.1.1 Nd:YLF Laser Pump

The first element of the transmitter is a Q-switched Nd:YLF laser pump system (Coherent Evolution 30 TEM<sub>00</sub> laser) with intra-cavity second harmonic

(527nm) generation. Using the  $\text{Nd}^{3+}:\text{YLiF}_4$  (Nd:YLF) as a gain medium provides several advantages when compared to other common neodymium type lasers such as Nd:YAG. One advantage is superior energy storage for high-pulse energy during Q-switched operations because of a long 470  $\mu\text{s}$  upper-state lifetime of the YLF.<sup>21</sup> Another advantage occurs during the operation of the laser. Nd:YLF lasers produce minimal thermal lensing and low, stress-induced birefringence.<sup>21</sup> This advantage allows scaling to higher laser powers while maintaining beam quality and efficiency. Moreover, the Nd:YLF exhibits relatively high thermal conductivity to allow efficient heat extraction. When Nd:YLF is brought together with efficient heat extraction and low birefringence, thermal depolarization issues found in optically isotropic materials such as Nd:YAG are practically eliminated.<sup>27</sup>

The Nd:YLF laser rod is contained within a laser diode pump chamber that is mounted in a mechanically indexed bracket to allow easy extraction and insertion of the pump chamber. The laser rod is held with o-rings in a water flow-tube that is surrounded by a gold-coated reflector with slits to transmit the pump light from the laser diodes into the Nd:YLF rod.

### **3.1.2 Diode Pumping**

The Nd:YLF laser pump utilizes laser diode pumping to provide optical excitation to the Nd:YLF gain medium. The use of laser diodes allows several

benefits over other pumping schemes. Compared to the broadband light emitted by conventional arc-lamps, the narrow spectral emission of the laser diodes permits very efficient pumping with most or all of the diode light remaining within the absorption band of the Nd:YLF gain medium.<sup>27</sup> As well, diode pumping results in minimal heat generation to allow low electrical and cooling utility requirements. Again, when compared to arc-lamps, diodes offer lifetimes with many thousands of hours while arc-lamps only last hundreds of hours.

A total of twelve AlGaAs laser diodes, arranged in three blocks of four high-powered diode bars, are employed to excite the laser gain medium. Each of the three blocks are electrically connected in series and mounted 120° apart down the length of the laser rod. All three blocks share electrical connections and a water-cooled heat sink to maintain temperatures.

### **3.1.3 Q-Switching**

The Nd:YLF laser pump utilizes an acousto-optic Q-switch to produce a pulsed laser output at a fixed repetition rate of 1 kHz. In acousto-optic Q-switching, an ultrasonic wave is sent into a block of transparent optical materials made of high-quality fused silica that is cut and polished to be optically oriented at Brewster's angle. The ultrasonic wave produces a photo-elastic effect in the fused silica block, thus resulting in an optical phase grating

within a period that is equal to the acoustic wavelength and an amplitude that is proportional to the sound amplitude. As the laser beam is incident upon the optical grating, the intensity of the laser beam is diffracted and deflected out of the laser cavity, thus allowing energy loss sufficient to reduce the Q (quality factor) of the laser cavity. As the ultrasonic energy is switched off, the laser is returned to the high Q-state and the fused silica block returns to a high state of optical transmission. During the state with no ultrasonic wave propagating through the fused silica block, the laser beam is no longer deflected and a Q-switched laser pulse is emitted.

The Q-switch is enclosed within a metal housing that is mounted on a riser block with a coarse azimuthal adjustment. Powering the Q-switch is an RF driver delivering approximately 30-40 Watts of RF power. The Q-switch is water-cooled with a built-in temperature interlock to switch off the RF power during an overheating condition.

#### **3.1.4 Intra-Cavity Frequency Doubling**

The Nd:YLF pump laser features intra-cavity, second harmonic generation. High conversion efficiencies require high-power densities and low divergence beams. Thus, a custom iris is mounted between the Q-switch and the Nd:YLF rod. This iris only allows the TEM<sub>00</sub> mode to lase within the cavity. To accommodate this, a non-linear doubling crystal is placed inside the laser

cavity. This solution subjects the non-linear crystal to high-circulating power that is necessary for efficient, second harmonic generation. A dichroic output mirror transmits the second harmonic wavelength (527-nm), while the fundamental wavelength (1053-nm) is reflected back in the laser cavity. The fundamental radiation is entirely contained within the laser cavity to be re-used for second harmonic generation. All lasing and second harmonic generation occurs between the cavity mirrors. After the 527-nm beam exits the laser cavity, a turning mirror reflects the beam out through a collimating lens.

The non-linear crystal used for second harmonic generation is a non-critical phase match  $\text{LiB}_3\text{O}_5$  (LBO) crystal that is characterized by good UV transparency, a relatively high optical damage threshold, and a moderate non-linear optical coefficient. In addition, the LBO crystal features chemical stability, mechanical hardness, and non-hygroscopic properties. These properties allow the LBO crystal to be a useful material for nonlinear optical frequency conversion. The LBO crystal is anti-reflection coated for both 1053-nm and 527-nm. In order to maintain the required temperature for non-critically phase match, the LBO crystal is mounted in a crystal housing designed to maintain set temperatures in the range of 157 to 171 degrees Celsius to within  $\pm 0.1$  degrees.

### 3.1.5 Ce:LiCAF Tunable UV Laser Head

The second element of the transmitter system is a custom-designed Ce:LiCaAlF<sub>6</sub> (Ce:LiCAF) tunable UV laser with an output range of 282-nm to 313-nm. An optical schematic of the Ce:LiCAF laser is shown in figure 15.

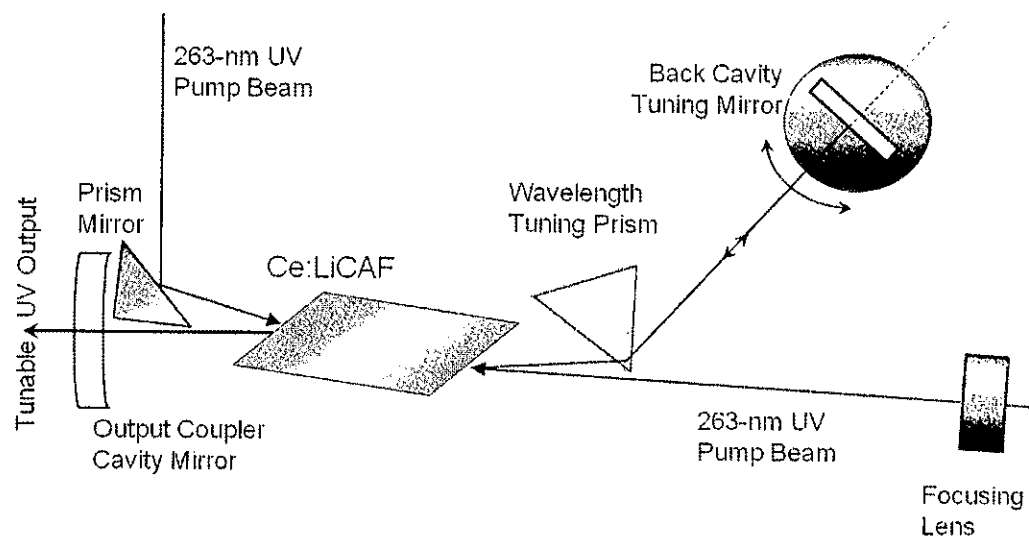


Figure 15: An optical schematic of the Ce:LiCAF UV laser tunable from 282 – 313 nm.

The Ce:LiCAF UV laser head receives the 527-nm output beam from the Evolution laser pump and pumps a CsLiB<sub>6</sub>O<sub>10</sub> (CLBO) crystal, with dimensions

of 5 mm x 5 mm x 10 mm (refer to figure 14). The CLBO doubles the frequency of the 527-nm green wavelength to the 263-nm ultraviolet wavelength or fourth harmonic of the Nd:YLF pump laser. The CLBO crystal is critically phase-matched and is set in an oven to maintain a temperature above 150°C to prevent hygroscopic damage. In addition, the CLBO oven is mounted on a rotation stage to angle tune the CLBO crystal for optimum phase matching, which results in high conversion efficiency. Following the harmonic conversion of the 527-nm pump beam into the 263-nm fourth harmonic, a dispersive prism is used to separate the 527-nm beam from the 263-nm UV beam. The 527-nm visible beam is transmitted into the atmosphere for aerosol measurements. The separated 263-nm beam is further divided into two separate beams using a beam splitter to pump the Ce:LiCAF crystal from opposite ends of the crystal. By double pumping the Ce:LiCAF crystal, a more uniform pumped volume is produced in the crystal.

### **3.1.6 Ce:LiCAF Wavelength Tuning**

In order to produce different wavelengths using a single laser, a high-reflective rear mirror is mounted on a servo-controlled galvanometer motor to allow rapid tuning of the output wavelength as shown in figure 15. The rapid tuning of this mirror moves the beam along an intra-cavity dispersing prism to produce discrete wavelengths between 282-nm to 313-nm for ozone



measurements. These wavelengths depend on the tuning mirror angle, which changes the position of the beam within the intra-cavity dispersing prism. To monitor the tunable UV wavelengths produced, a high-resolution spectrometer receives a portion of the tunable UV transmission through a fiber optic cable located at the back of the tuning cavity mirror. The position of the output beam from the Ce:LiCAF cavity does not change, as the laser is wavelength tuned.

In order to maintain a constant temperature of the Ce:LiCAF laser crystal during pumping, the crystal is mounted in a copper mount on top of a water cooled heat sink. The entire crystal assembly is further mounted on a motorized stage that translates the laser crystal when needed. After prolonged periods of laser operation, solarization may occur on part of the crystal subjected to high UV pump fluence, which can gradually reduce the output energy.<sup>28</sup> To recover the output energy, the Ce:LiCAF crystal is repositioned to utilize a fresh part of the crystal.

### **3.1.7 Transmitter Optics**

As the output of the Ce:LiCAF UV laser (~290-nm) and the visible green beam (527-nm) exits the transmitter, the beams are directed to a set of beam expanders to reduce divergence. The UV beam and visible beams are directed to a 5x beam expander and 3x beam expander, respectively. The beam expanders are designed to keep the transmitted beams to a diameter of

approximately 0.5-mm with a beam divergence of  $<0.3$  mrad. After the beam expanders, both expanded output beams are subsequently directed to a motorized mirror next to the telescope, which allows the atmospheric beams to be aligned with the stationary receiver telescope.

### **3.2 Receiver System**

The lidar receiver system consists of a receiver telescope with a 40-cm diameter primary mirror with an F number of  $F/1.8$  and a focal length of 731.5-mm. An optical schematic of the telescope assembly is shown in figure 16. A negative lens was added to the receiver to reduce the telescope F number to  $F/2.46$  to obtain a 1-m effective focal length. Connecting the telescope to the detection array is a Thorlabs (FTO38MM) UV fiber optic cable with a numerical aperture of 0.22 that transmits the received signal from the telescope to the receiver box, which houses the detectors.

#### **3.2.1 Detection Array**

A receiver box houses the detection array that employs three detection channels. Figure 17 illustrates an optical schematic of the receiver box. Two photomultiplier tubes (PMT) manufactured by Hamamatsu (R7400) are used for collection of the near- and far-field UV signals and one avalanche

photo diode (APD) manufactured by Perkin & Elmer (C3095E-TC) is used for the collection of the visible green (527-nm) signal. After the fiber optic cable delivers the signal received by the telescope, a beam splitter divides the signal into the green and UV beams. The green beam passes through a narrowband pass filter and is directed to the APD for signal detection. A focusing lens assembly directs the visible signal into the small area APD which is also connected to a transimpedance amplifier. The UV signal is sent through a UV broadband filter (both on- and off-line wavelengths) and is further divided using a second beam splitter to send approximately 90% of the UV return signals to the far-field PMT for signal detection with the remaining 10% of the UV return signals and is then sent to the near-field PMT for signal detection. Each of the UV return signals is directed into the PMTs using a UV focusing lens to be processed.

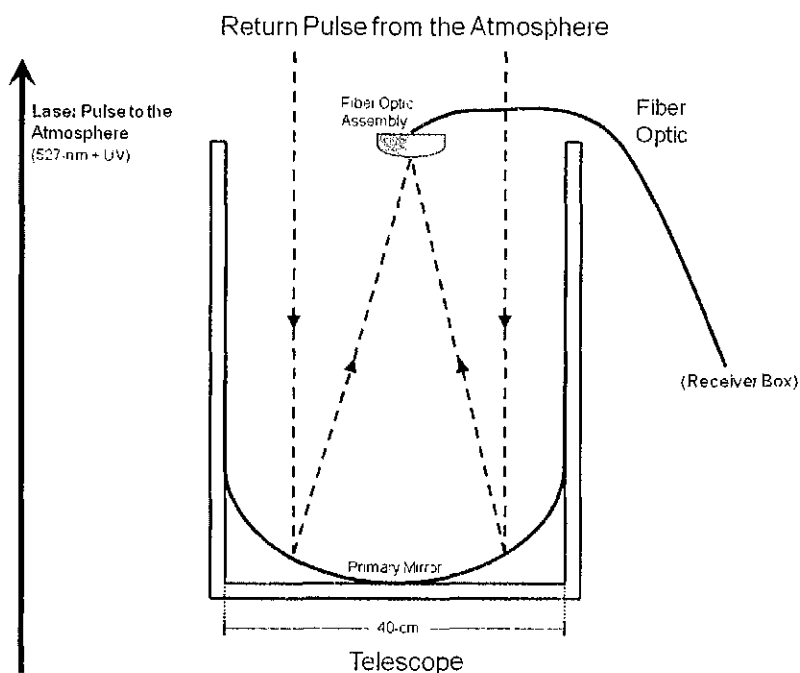


Figure 16: Optical schematic of the telescope assembly.

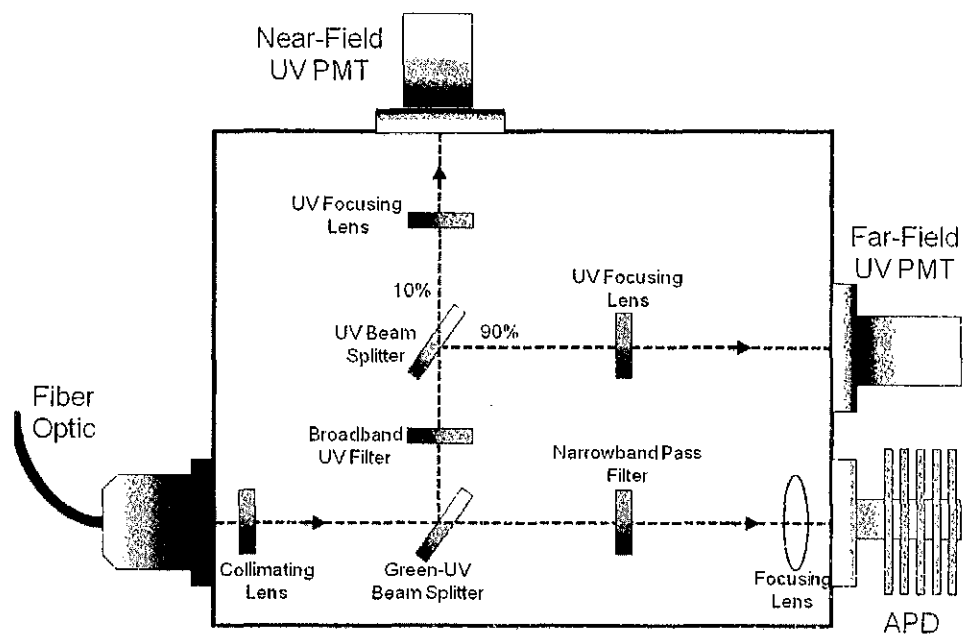


Figure 17: Optical schematic of the receiver box.

### 3.3 Lidar Control and Support

The system requires various components for lidar control and support. A schematic of the complete lidar system can again be found in figure 13.

Many of the lidar control and support units are located on a system rack beginning with an industrial Pentium IV computer with an LCD screen and a built-in keyboard/mouse. The computer handles lidar control, data acquisition, and analysis. Next, a custom General Control Unit (GCU) module aids in the control and operations for both the Nd:YLF pump laser and Ce:LiCAF UV laser head. The GCU contains a master clock for the timing transmitter sequences, the switching between the on-line and off-line wavelengths, the data acquisition system, and the operation of the energy and wavelength monitors. Also within the GCU are several other support components such as an Ocean Optics high-resolution UV spectrometer, CLBO temperature controller, and various motor controllers. The rack also houses a 1000VA uninterruptible power supply (UPS) that maintains power to the LBO and CLBO crystals, the Licel Transient Digitizer, and the Nd:YLF laser power supply with an onboard temperature controller for the LBO crystal.

Tasked with cooling the lidar system is a separate, free-standing closed-loop chiller with various control options set to maintain an operational system temperature of approximately 27°C. The chiller is designed to dissipate the

waste heat generated and maintain the wavelength of the laser diodes by maintaining a constant temperature. This ensures the maximum absorption of the diode energy by the Nd:YLF gain medium. To reduce corrosion and algae growth within the system, a chemical additive is included in the water system.

The lidar control software is a National Instruments CVI/Lab windows-based package, which allows graphical user-interface for easy operations of menu-driven controls to configure the lidar for different operational modes. The lidar parameters include integration time, selection of on-line and off-line wavelengths, and background signal collection. The software includes a program for real-time display of the lidar signal and the display of the ozone concentration calculated from atmospheric measurements.

### **3.4 Data Acquisition System**

The data acquisition system consists of two main parts. The first part consists of a Licel Transient Digitizer for far-field UV detection which contains a 250 MHz fast photon counting system and powerful analog-to-digital (A/D) converters (12-bits at 40 MHz). The Licel Digitizer is triggered by two inputs that allow data acquisition of two repetitive channels (on-line and off-line). All data is collected at 1 KHz with 500 Hz each for the on-line and off-line signals. Additionally, two separate onboard RAM modules permit the separate signals to

be added sequentially with 10 acquisition data files saved every second. The second part involves two data acquisition (DAQ) boards (NI 6115) from National Instruments (NI). The NI-DAQ boards perform high-speed, analog data acquisition for the near field UV and visible signals and have four channels each with 12-bit resolution, and 10 MS/s per channel. The two National Instrument boards are configured in a “ping-pong” mode in order to record signals without losing any data. As one of the boards acquires data, the other board saves the acquired data then waits for a trigger to continue data acquisition. Each board acquires four seconds of data (4 x 1000 shots) and then processes the data in the following four seconds as the other board obtains data. Lastly, the data is saved sequentially as a ten shot average over a span of 10 milliseconds.

### **3.5 Atmospheric Transmission Setup**

A basic diagram of the ground-based, atmospheric transmission setup is shown in figure 18. To obtain an ozone atmospheric measurement, the transmitter sends a laser pulse into the atmosphere at alternating on-line and off-line wavelengths. The 527-nm green laser output is always transmitted giving a return from atmospheric aerosols. The telescope collects the returned laser pulse from the atmosphere and sends the return signal to the detector box

using a fiber optic. Within the detector box, the PMTs detect signals for the near- and far-field returns and an APD is used for the detection of the visible aerosol return signal.

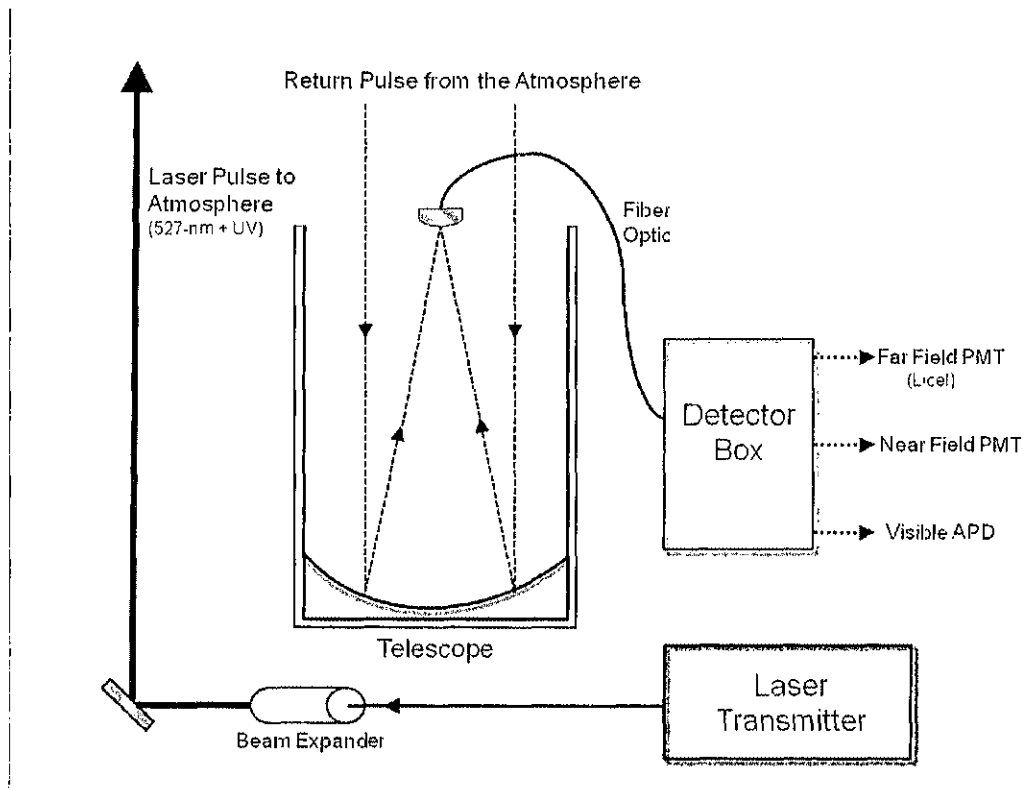


Figure 18: Lidar setup for atmospheric ozone measurements.



## CHAPTER IV

### ATMOSPHERIC OZONE LIDAR CALCULATION

In this chapter, an ozone calculation will be made using the lidar and DIAL equations shown in equations (13) and (30). In considering a two-component atmosphere with the effects caused by molecules and aerosols, the backscatter  $\beta$  and extinction  $\alpha$  coefficients are the unknown variables in the lidar equation. In addition, this chapter provides theoretical calculations to simulate the lidar return signal based on the lidar system parameters addressed in this thesis by using various atmospheric models to determine the backscatter and extinction variables.

#### 4.1 Backscatter Coefficients

Two approaches were used to determine the backscatter coefficient used in the lidar return calculation. The first approach involves a computer program, LIDAR-PC, which is a computer program that is designed to simulate the laser return of the atmosphere based on the associated atmospheric spectral databases.<sup>29</sup> The program allows various atmospheric parameters to be inputted to model the atmosphere. In determining the backscatter coefficients as a function of range, both molecules and aerosols were considered.

The second approach involves backscattering from gas molecules only and is solely dependent on the density of the atmosphere. This is a worst-case analysis as the actual return power should be greater due to aerosol backscattering. The molecular density of gas molecules is a function of altitude (range) and decreases as the altitude increases. Gas molecules are very small compared to the DIAL wavelengths used in remote sensing. Therefore, the theoretical equation used to determine the molecular backscattering  $\beta_g$  is the Rayleigh scattering approximation shown in equation (39). Hence,<sup>30</sup>

$$\beta_g = N_g \frac{d\sigma_R(\pi)}{d\Omega} \quad (39)$$

where  $N_g$  is the number of atmospheric gas molecules per unit volume and  $d\sigma_R(\pi)/d\Omega$  is the differential Rayleigh scattering cross section at scattering angle  $\theta = \pi$  per gas molecule. At altitudes below 100 km where the mixing of atmospheric gases occur, equation (40) describes the differential Rayleigh scattering cross section.<sup>30</sup>

$$\frac{d\sigma_R(\pi)}{d\Omega} = 5.45 \left[ \frac{\lambda(\mu m)}{0.55} \right]^{-4} \times 10^{-32} m^2 sr^{-1} \quad (40)$$

Therefore, the following theoretical equation (41) is used to calculate the molecular backscattering when  $N_g$  is number per  $m^3$ .

$$\beta_g = N_g \cdot 5.45 \left[ \frac{\lambda(\mu m)}{0.55} \right]^{-4} \times 10^{-32} m^{-1} sr^{-1} \quad (41)$$

## 4.2 Extinction Coefficient

Again, two approaches were used to determine the extinction coefficient used in the theoretical lidar return calculation.

The first approach involves an atmospheric extinction model based on scattering from aerosols, molecules, and ozone absorption. The atmospheric model was developed by the Air Force Cambridge Research Laboratories in which the optical parameters were computed spectrally and is sufficient for exploratory calculations.<sup>31</sup> Based on this model, the extinction coefficients as a function of altitude were used to calculate the lidar return.

The second approach involves extinction from gas molecules only. The extinction coefficient  $\alpha_g$  from gas molecules contains both elastic and inelastic components; however, the inelastic component is several orders of magnitude

smaller and is usually neglected.<sup>30</sup> As stated earlier, gas molecules are very small compared to the DIAL laser wavelengths. Therefore, the elastic scattering by gas molecules can be expressed by the Rayleigh scattering cross-section  $\sigma_R$ . Thus, the gas extinction coefficient can be expressed as seen in equation (42)

$$\alpha_g = N_g \sigma_R \quad (42)$$

where  $N_g$  is the number of gas molecules per unit volume. For altitudes below 100 km, the atmospheric Rayleigh cross-section for a given wavelength is given by equation (43).<sup>30</sup>

$$\sigma_R = 4.56 \left[ \frac{\lambda(\mu m)}{0.55} \right]^{-4} \times 10^{-31} m^2 \quad (43)$$

As a result, the theoretical equation used to calculate the extinction coefficient from gas molecules is shown in equation (44). Extinction from ozone absorption is not considered here.

$$\alpha_s = N_s 4.56 \left[ \frac{\lambda(\mu m)}{0.55} \right]^{-4} \times 10^{-31} m^{-1} \quad (44)$$

### 4.3 Lidar Calculation

Using the more general form of the lidar equation and shown again in equation (45),

$$P(R) = P_0 \beta(\lambda, \theta, R) \frac{c \tau}{2} \frac{A}{R^2} \eta(\lambda) G(R) T^2(\lambda, R) \quad (45)$$

two sets are lidar returns that were calculated and graphed based on the backscatter and extinction coefficients discussed above. The graphed results are illustrated in figure 19.

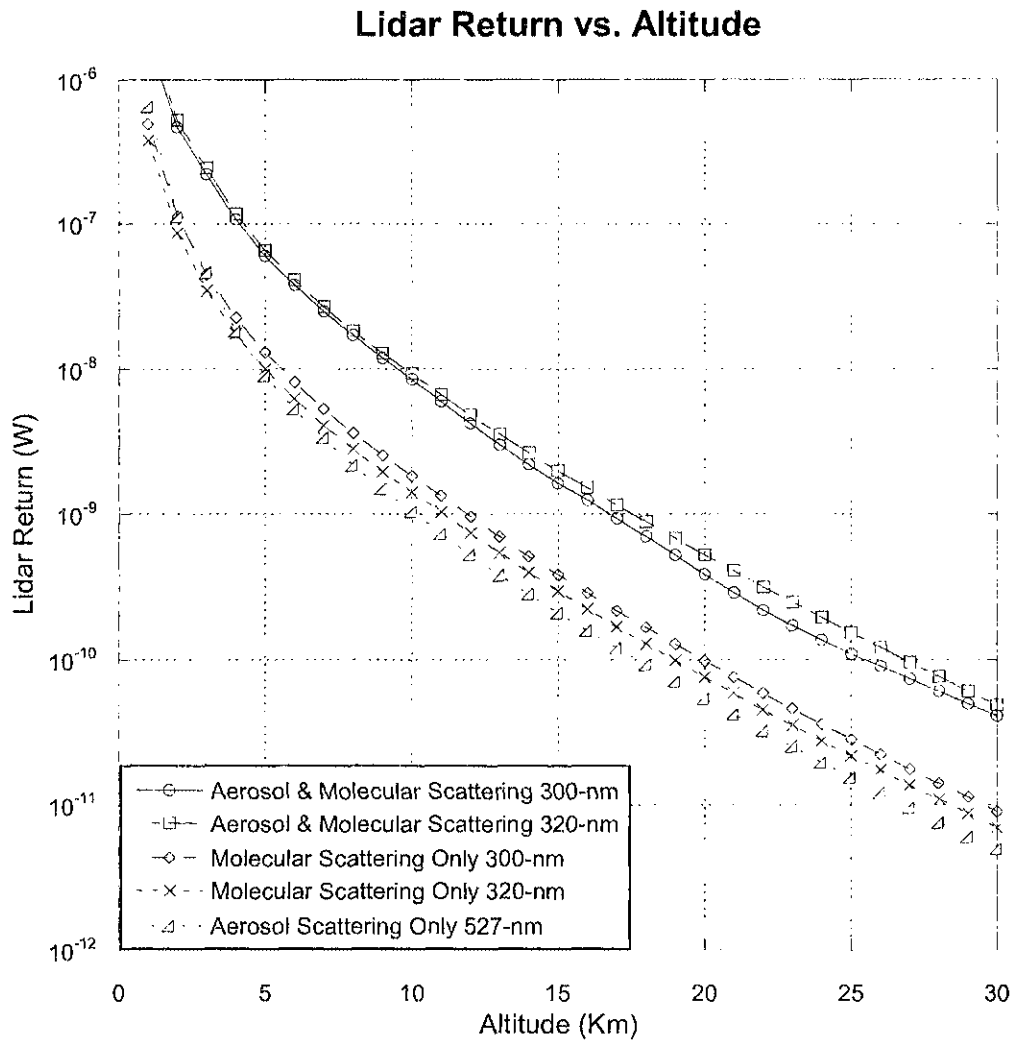


Figure 19: Theoretical calculation of a lidar return.

The remaining variables are a function of the lidar system and are known. The values used in the lidar calculation are shown in table 1 with the backscatter and extinction coefficients based on the data (aerosol and molecular scattering) and equations (molecular scattering only) which were discussed earlier.

Table 1: Lidar equation values.

Lidar Parameters	Value
Power transmitted, $P_0$	90000 W
Effective spatial pulse length, $c\tau/2$	1000 m
Telescope Area, A	0.50 m <sup>2</sup>
Receiver Efficiency, $\eta(\lambda)$	0.50
Overlap, G(R)	1

The two DIAL wavelengths used were 300-nm for the on-line wavelength and 320-nm for the off-line wavelength. These wavelengths were chosen because extinction data was available. The first set of lidar returns were calculated while considering aerosol and molecular atmospheric models for the backscattering coefficients and extinction coefficients. As seen in figure 19, the lidar return for the off-line wavelength 320-nm has a higher overall power when compared to the on-line wavelength, which is more absorbed by ozone. The second set of lidar returns were calculated only after considering molecular atmospheric models for the backscattering coefficients and extinction coefficients. Again, the lidar return based on the off-line wavelength showed a higher power lidar return. In addition, the lidar returns based on a molecular atmospheric model showed a lower overall power return due to the fact that aerosols were not considered in the calculation. With a higher concentration of aerosols, a greater lidar return is achieved.

In addition, a lidar return was calculated using a 527-nm wavelength to determine the aerosol concentration in the atmosphere. The Lidar-PC program was used to determine the backscattering and extinction coefficients used in the lidar equation. At this particular wavelength, there is no ozone absorption (see figure 8).

#### 4.4 DIAL Calculation

By inputting the lidar returns for each of the on-line and off-line wavelengths, ozone concentration as a function of range can be calculated using the DIAL equation as discussed in section 2.3. The DIAL equation is shown again in equation (46).

$$N(R) = \frac{1}{2\Delta\sigma\Delta R} \ln \left[ \frac{P(\lambda_{on}, R_1)P(\lambda_{off}, R_2)}{P(\lambda_{off}, R_1)P(\lambda_{on}, R_2)} \right] \quad (46)$$

This form of the DIAL equation provides a method of calculating atmospheric ozone as a function of range. The concentration of ozone is determined by the natural logarithm of the received powers for the on-line and off-line wavelengths for a given range cell  $\Delta R = (R_2 - R_1)$ , in this case is 1000-m. The difference



between the ozone absorption cross-section  $\Delta\sigma$  at the on-line and off-line wavelengths is  $33.3 \times 10^{-24} \text{ m}^2$ . The calculated DIAL results are shown in figure 20. The graph illustrates a typical DIAL graph showing ozone concentrations in the stratosphere and troposphere with the bulk of the ozone concentration in the stratosphere.

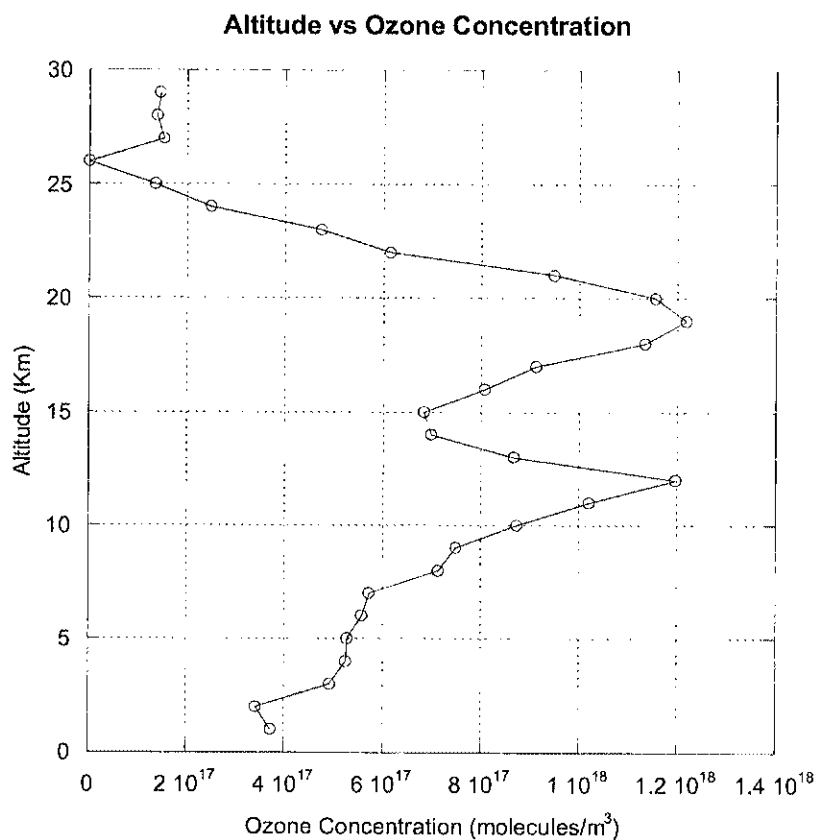


Figure 20: Calculated DIAL results.

## CHAPTER V

### AEROSOL LIDAR SYSTEM RESULTS

In this chapter, measurements were conducted on the lidar system to characterize the system performance. In addition, the lidar system was used to perform atmospheric measurements using the 527-nm aerosol channel. Lastly, the results from the lidar system measurements and the atmospheric measurements are presented.

#### 5.1 Nd:YLF Pump Laser

The first component of the lidar transmitter is a Q-switched Nd:YLF laser pump system (Coherent Evolution 30 TEM<sub>00</sub> laser) with intra-cavity second harmonic 527-nm generation, refer to figure 14. This laser pump system operates at a constant 1 KHz to achieve a stable thermal lens in the YLF crystal. Thermal lensing happens as a temperature gradient occurs in the gain medium as the volume along the beam axis is heated. All measurements are taken at 1 KHz repetition rate.

The Nd:YLF laser pump utilizes laser diode pumping to provide optical excitation of the Nd:YLF gain medium. A closed loop chiller is used both to maintain the temperature and thus the laser diode wavelength (diode emission

is temperature dependent) and to ensure maximum absorption of the diode pump energy into the Nd:YLF laser rod. Using an energy meter, the 527-nm output was measured as a function of the chiller temperature to determine the optimum temperature required to produce the maximum 527-nm output at a diode current of 15 amps. At higher diode currents, the results are similar. A graph of the result is shown in figure 21.

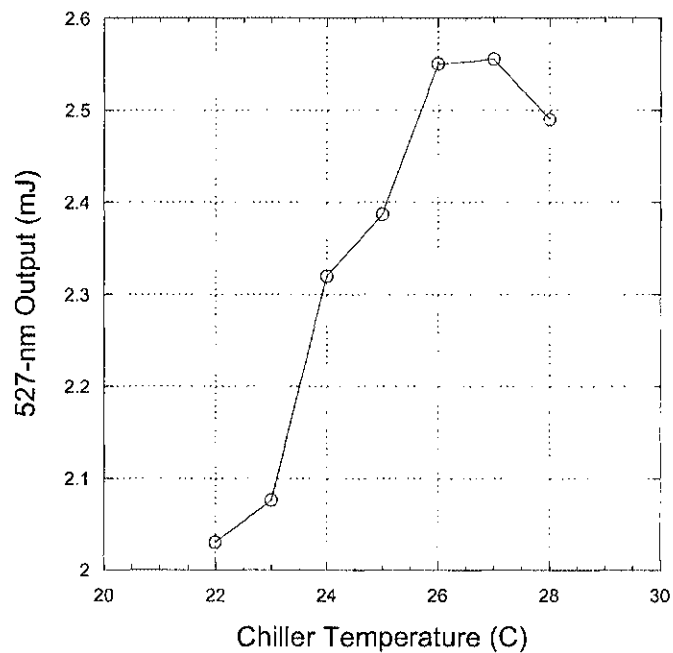


Figure 21: The 527-nm laser output as a function of chiller temperature (diode current: 15 amps).

As shown from the graph, the chiller temperature of 27°C provided the maximum diode energy absorption.

An intra-cavity non-linear LBO crystal is used to produce the second harmonic 527-nm energy within the laser cavity. The LBO crystal is a non-critical phase match crystal that is temperature tuned for optimum, phase matched, second harmonic generation. The 527-nm laser pump output was measured using an energy meter as a function of LBO oven temperature and graphed in figure 22.

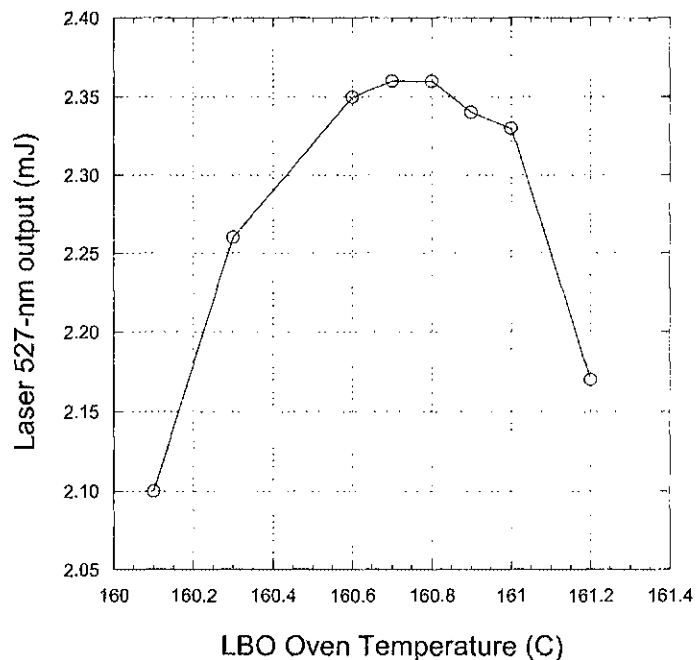


Figure 22: The 527-nm laser pump output as a function of LBO oven temperature (diode current: 15 amps, chiller temperature: 27 °C).

From the results, the optimum LBO oven temperature is 160.6°C for maximum second harmonic 527-nm generation.

Varying the current supplied to the laser diodes, which pump the Nd:YLF rod, allows control of the 527-nm output energy. The 527-nm output energy was measured using an energy meter as a function of diode current. The graph of the result from the measured output is shown in figure 23.

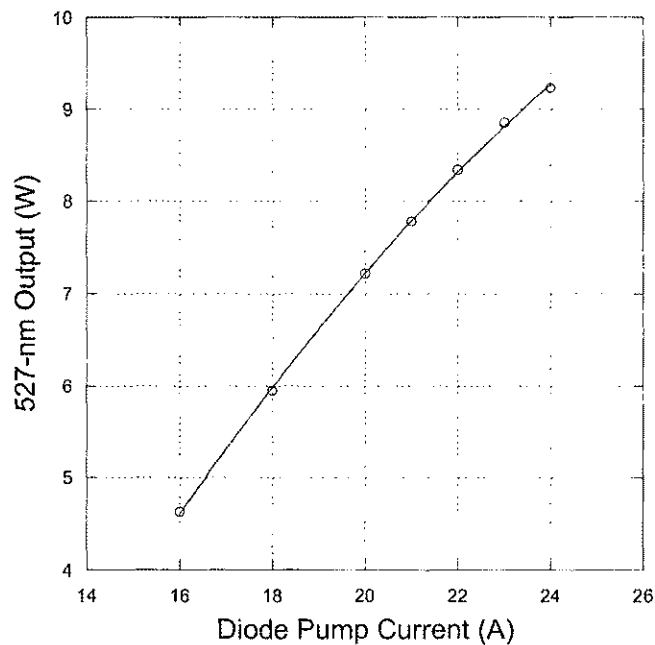


Figure 23: 527-nm laser pump output as a function of diode current.

The graph of the 527-nm pump energy as a function of diode current in figure 23 indicates a maximum energy of 9.23 mJ at 1 KHz with a diode current of 24

amps. The 527-nm pump energy at 24 amps according the manufacture's specifications is approximately 11 mJ at 1 KHz. This energy is now used to pump a CLBO crystal to generate fourth harmonic 263-nm energy.

Using a beam grabber with a CCD camera, the beam profile of the 527-nm was Gaussian with an observed single elliptical shape, TEM<sub>00</sub> mode. The measured dimensions of the beam profile are 227- $\mu$ m in the x-axis and 195- $\mu$ m in the y-axis.

Using an oscilloscope and pin diode, the FWHM (full-width half-maximum) of the fundamental wavelength (1053-nm) and the second harmonic wavelength (527-nm) was measured. The FWHM of the fundamental and second harmonic wavelength was measured to be 220-ns and 107-ns at 24 amps, respectively. In addition, the pulse stability of the 527-nm wavelength was determined by measuring the height of 100 pulses. The difference between the maximum and minimum value was less than 6%.

## **5.2 Fourth Harmonic Generation**

A waveplate changes the horizontally polarized 527-nm output beam into a vertically polarized beam before it pumps the CLBO crystal, with dimensions of 5 mm x 5 mm x 10 mm, shown in figure 14. The CLBO crystal doubles the frequency of the input 527-nm green wavelength to the 263-nm ultraviolet

wavelength or fourth harmonic of the Nd:YLF laser. The CLBO crystal is critically phase-matched and is set in an oven to maintain a temperature above 150°C to prevent hygroscopic crystal damage. To facilitate phase matching, the CLBO crystal is angle tuned approximately three degrees ( $\pm 0.5^\circ$ ) horizontally to optimize the fourth harmonic 263-nm generation. In order to determine the amount of fourth harmonic 263-nm energy generated, an energy meter was used to measure the amount of 263-nm energy produced as a function of input 527-nm pump energy. The graph of the result is shown in figure 24.

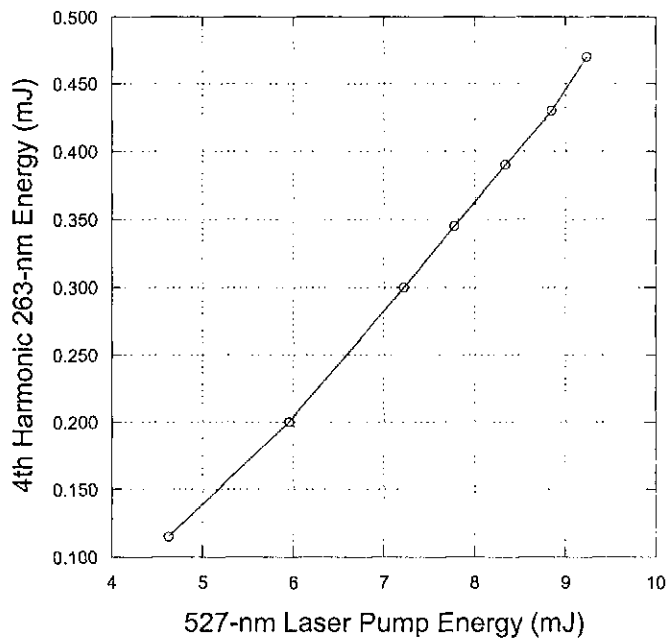


Figure 24: Fourth harmonic 263-nm generation as a function 527-nm laser pump energy.

In figure 24, the graph indicates a maximum of 0.470 mJ of 263-nm energy at approximately 9.23 mJ of 527-nm energy. In addition, to determine the relationship between the amount of 527-nm energy incident on the CLBO crystal and the generation of 263-nm energy, the conversion efficiency,  $\eta$ , for the fourth harmonic 263-nm generation was calculated and graphed in figure 25.

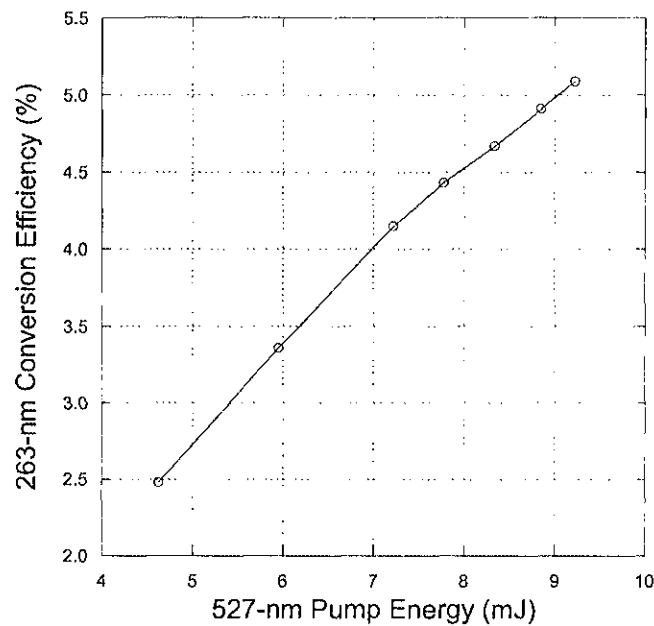


Figure 25: Four harmonic conversion efficiency as a function of 527-nm pump energy.



In figure 25, the graph indicates a maximum 263-nm conversion efficiency  $\eta$  of approximately 5.1%. Experimental conversion efficiencies for a 10-mm CLBO crystal can be as high as 44%.<sup>32</sup> The measured conversion efficiencies,  $\eta$ , of 263-nm generation are compared with theoretical calculations using equation (38) as illustrated and discussed in chapter 2. This equation is used to approximate the harmonic conversion efficiency and for reference is shown again in equation (47)<sup>25</sup>

$$\eta = \frac{P_{2\omega}}{P_{\omega}} = l^2 K \frac{P_{\omega}}{A} \text{sinc}^2\left(\frac{\Delta k l}{2}\right) \quad (47)$$

where

$P_{2\omega}$	Power is generated at second harmonic wavelength
$P_{\omega}$	Input power incident on the crystal
$l$	Length of CLBO crystal, 10-mm
$K$	Nonlinear coefficient for the CLBO crystal, $6.97 \times 10^{-11} \text{ W}^{-1}$
$A$	Area of the input beam, $1.39 \times 10^{-7} \text{ m}^2$
$\Delta k$	Phase mismatch between the polarization wave and electromagnetic wave, $\Delta k = 0$

The theoretical result was based on the assumption of zero phase mismatch ( $\Delta l = 0$ ). Additionally, a beam profiler and camera was used to measure the beam profile of the 527-nm pump energy and verified the laser pump is lasing in the TEM<sub>00</sub> mode. The area of the input beam is  $1.39 \times 10^{-7} \text{ m}^2$ . The theoretical conversion efficiencies were calculated based on 10-mm and 15-mm long CLBO crystals. The original 15-mm crystal was damaged and only a 10-mm crystal was available for this test. The theoretical conversion efficiencies along with the measured conversion efficiencies are shown in figure 26 with a summary of the results and parameters in table 1. The graph illustrates the benefit of a 15-mm CLBO crystal in generating higher amounts of 263-nm energy.

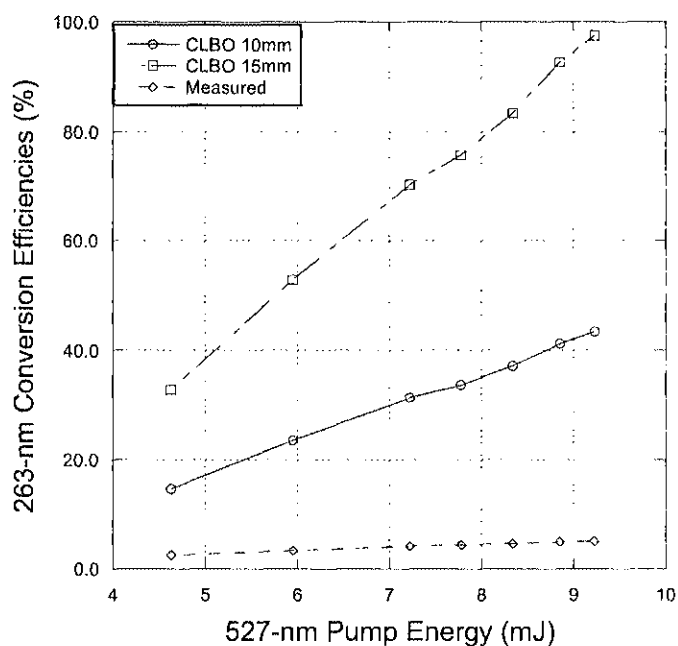


Figure 26: Measured and theoretical conversion efficiency (263-nm).

Table 2: Summary of values used to determine 4th Harmonic generation.

527-nm Energy (mJ)	FWHM (ns)	Power in (W)	Measured, $\eta$	CLBO 10-mm, $\eta$	CLBO 15-mm, $\eta$
4.63	159	29119	0.0248	0.146	0.329
5.95	127	46850	0.0336	0.236	0.529
7.22	116	62241	0.0415	0.313	0.703
7.78	116	67069	0.0443	0.337	0.758
8.34	113	73805	0.0467	0.371	0.834
8.85	108	81944	0.0485	0.412	0.926
9.23	107	86262	0.0509	0.434	0.975

Compared to the theoretical 263-nm conversion efficiencies, the measured result is substantially low. Only a used 10-mm CLBO crystal was available for this test. The condition of the CLBO crystal was the main reason for the low 263-nm conversion efficiency. The installed CLBO crystal had visible clouding on the crystal faces due to hygroscopic damage. This increased the absorption and scattering of the input 527-nm pump energy within the CLBO crystal, which reduced the amount of pump energy available for conversion.

Using an oscilloscope and pin diode, the FWHM of the fourth harmonic wavelength (263-nm) was measured. The FWHM of the 263-nm wavelength was measured to be 68-ns at 24 amps.

The 263-nm energy is used to pump the Ce:LiCAF crystal to produce tunable UV wavelengths. According to design specifications, the Ce:LiCAF crystal requires a threshold energy of approximately 400  $\mu\text{J}$  to produce tunable UV wavelengths. Currently, the system generates a maximum of 470  $\mu\text{J}$  of 263-nm energy at 24 amps (refer to figure 24). The 470  $\mu\text{J}$  of 263-nm energy is marginally above threshold and with possible issues in system alignment a higher amount of 263-nm energy is needed to produce tunable UV wavelengths from the Ce:LiCAF crystal.

Attempts were made to produce tunable UV wavelengths from the Ce:LiCAF, however, none were generated. The two 263-nm pump beams were optimized to ensure the same volume was being pumped within the Ce:LiCAF crystal, see figure 15. Furthermore, the output coupler was adjusted to facilitate lasing within the Ce:LiCAF cavity with no result. These efforts produced no tunable UV wavelengths within Ce:LiCAF cavity as viewed through a spectrometer.

### **5.3 Receiver Efficiency**

The efficiency of the receiver box was determined using a small 532-nm CW diode laser and an oscilloscope with a large area pin diode. An aperture with a diameter of approximately 0.5 mm was installed on the diode laser to

ensure the signal is transmitted completely through the telescope fiber optic to the receiver box and then to the APD (refer to figure 17). In addition, a special KG-3 filter was used to block the 1064-nm wavelength component of the small diode laser and allowed only the transmission of the 532-nm wavelength. The oscilloscope with a pin diode measured the relative intensity of the CW diode laser at the input of the fiber optic and at the input of the APD. Receiver box efficiency from the input of the fiber optic to the APD is measured to be approximately 93%. The measured efficiency does not include the 527-nm narrow band filter which has transmission efficiencies of 50%. The telescope design specification sets the efficiency of the telescope at 92%. The total receiver system efficiency is defined as  $\text{Efficiency}_{\text{receiver}} = (\text{efficiency}_{\text{telescope}})(\text{Narrowband optical filter})(\text{fiber optic})$ . Therefore, the total receiver system efficiency is approximately 43%.

In addition, a conversion factor, V/W (voltage per watt), was measured in order to help convert the raw data expressed in voltage by the data acquisition system into power as seen by the APD. This will allow a proper comparison between the measured and theoretical results. The APD with the trans-impedance amplifier was treated as one device or "blackbox." A small 532-nm CW diode laser with a neutral density filter was used to input approximately 1.6  $\mu\text{W}$  of CW power into telescope fiber optic to incident onto the APD. The 527-nm narrowband filter was removed to allow the 532-nm energy to reach the APD. Using an oscilloscope, a change in voltage at the output of the trans-

impedance amplifier was measured to be 7.4 V. Accounting for the loss through the fiber optic to the APD, approximately 1.5  $\mu\text{W}$  of CW power reached the APD. The conversion factor is defined as a ratio of volts to watts and is calculated to be 5 MV/W.

#### **5.4 527-nm Atmospheric Aerosol Test**

The 527-nm visible pump beam was transmitted into the atmosphere at 1 KHz with a pulse energy of approximately 3 mJ. In the receiver box (refer to figure 17), the backscattered signal was detected by the APD with a voltage of 300 V on January 8, 2009 at approximately 1:00 PM. The return profile is graphed in figure 27. The graph displays a ten pulse average that occurred during a span of 10 milliseconds. In figure 27, the two graphs show that the background-subtracted range corrected backscattered energy from the lidar transmission at altitudes associated with the boundary layer and troposphere.

In figure 27(a), the overlap function (refer to equation (13)) occurs from ground level to an altitude of approximately 150-m. At low altitudes, the laser beam is not in the telescope's field-of-view (FOV); however, as the beam travels through the atmosphere, the laser beam gradually begins to overlap the telescope's FOV. At approximately 150-m high, the beam is entirely in the telescope's FOV. At this altitude, the transmitted laser beam completely

overlaps the telescope's FOV and the overlap function is 1. The region before complete overlap occurs is avoided because problems occur in processing data and is generally avoided for this reason.<sup>12</sup> Reliable data is obtained after complete overlap occurs.

During this particular day, the boundary layer, which is a sub-layer of the troposphere, is located at approximately 500-m, refer to figure 27(a). This particular day was very overcast with low-lying clouds. The large return shown in the graph shows a low-flying cloud at an altitude of 500-m. This is the height of the boundary layer that contains molecules as well as aerosols. Above an altitude of 500-m, the return signal is reduced because only molecular scattering occurs above the boundary layer. At altitudes above the boundary layer, little to no aerosol scattering occurs. A reduced return occurred at an altitude of 800-m which indicated a possible cloud above the boundary layer; however, the return signal was attenuated due to the low-flying cloud blocking the return signal.

The backscattered signal falls off as  $1/R^2$ , as implied by equation (13), and must be range corrected by multiplying the backscattered signal by  $R^2$ . In addition, the signal is noise corrected by subtracting a DC noise level to reduce the affects of noise as the signal is range corrected. The effect of imperfect noise subtraction increases dramatically with  $R^2$  as seen in figure 27(b) with the signal deviating as altitude increases.

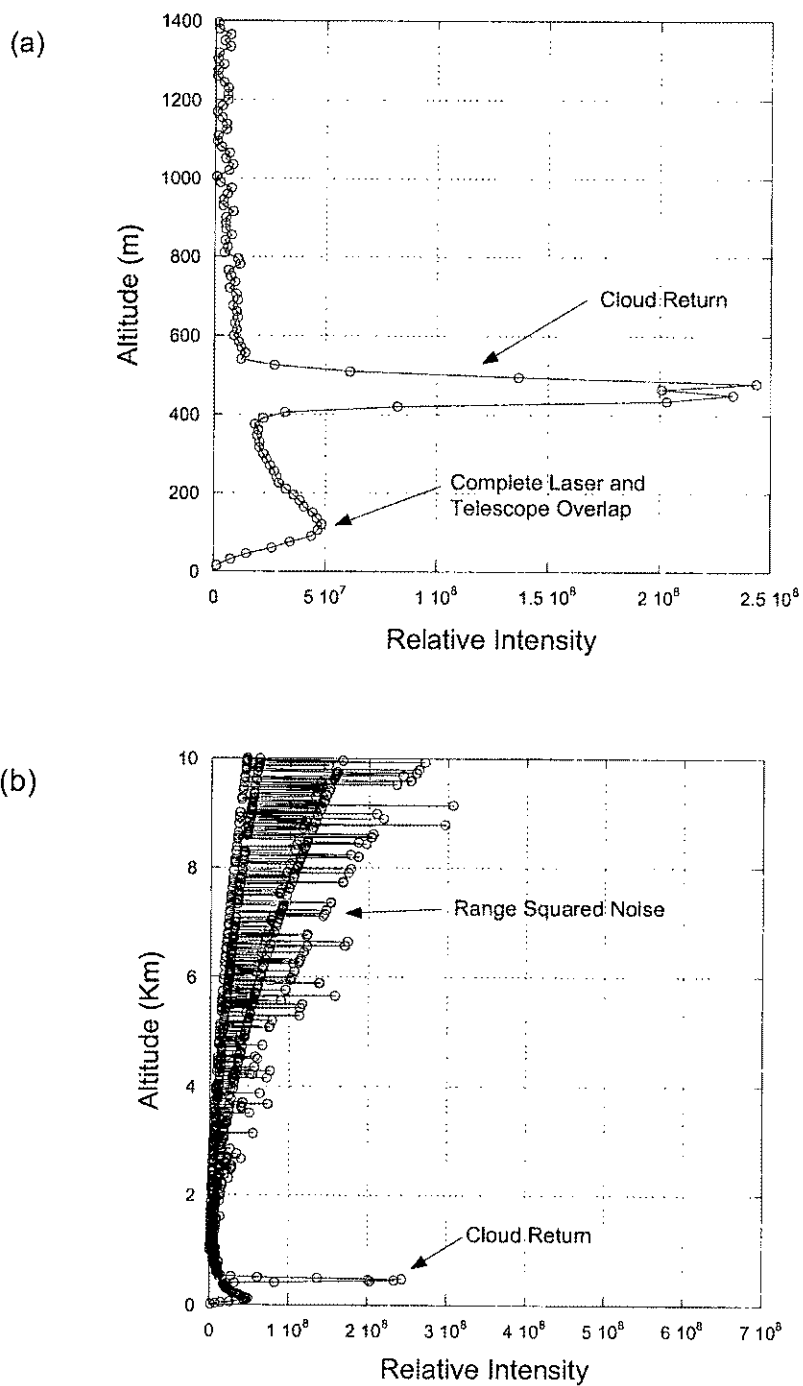


Figure 27: Lidar backscatter results from the transmission of the 527-nm beam for (a) 0-1400 m and (b) troposphere (0-10 Km).



An example of a return profile with no large cloud return taken on the same day is shown in figure 28. The return profile was detected by the APD with a voltage of 300 V and displays a ten pulse average that occurred during a span of 10 milliseconds.

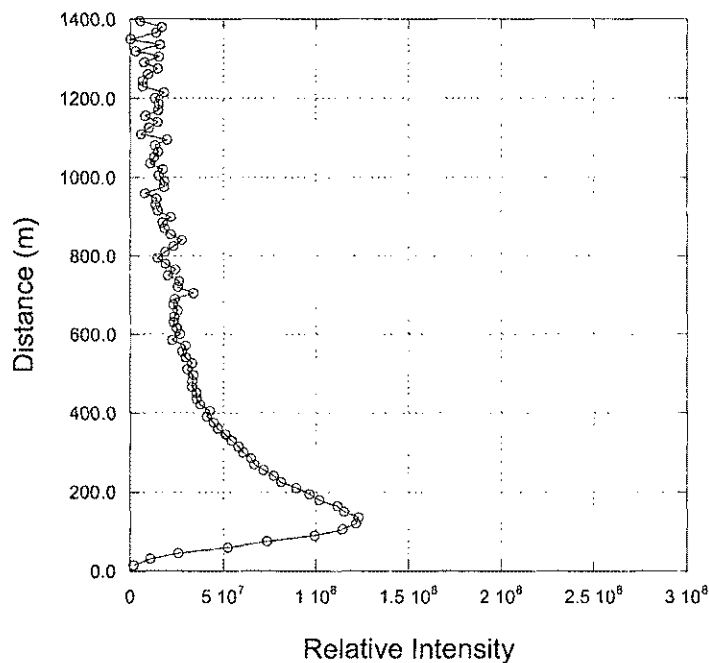


Figure 28: Lidar backscatter from the transmission of the 527-nm beam.

## CHAPTER VI

### DISCUSSION

This chapter discusses the results obtained to characterize the lidar system. From these results, various parameters were adjusted to optimize the lidar system for maximum operational efficiency. In addition, the experimental results of the transmitted 527-nm visible beam and theoretical results of the lidar equation are compared.

The lidar system requires a cooling system in order to manage heat generated during the operation of the system. More importantly, the closed loop cooling system maintains both system temperatures and the laser diode wavelength in order to ensure maximum absorption of the diode pump energy into the Nd:YLF laser rod. A chiller of temperature of 27°C was measured to provide the optimum temperature for maximum diode pump energy.

The laser pump utilizes an intra-cavity, non-linear LBO crystal to produce the second harmonic 527-nm energy within the laser cavity. The LBO crystal is a non-critical phase matched crystal and is temperature tuned for maximum second harmonic generation. An LBO oven temperature of 160.6°C produced the maximum amount of 527-nm energy. With the chiller and LBO oven temperature optimized, a maximum of 9.23 mJ of 527-nm energy was measured at a diode pump current of 24 amps (maximum recommended).

Design specifications for the laser pump show a maximum energy of 11.2 mJ at 24 amps. This energy is used to pump the CLBO crystal within the Ce:LiCAF laser. Furthermore, the design specification requires approximately 4.5 mJ of 527-nm energy to generate enough fourth harmonic 263-nm light to reach the threshold energy to pump the Ce:LiCAF laser. Even though the pump laser produces approximately 18% less than design specifications, the laser pump produces sufficient 527-nm energy to produce tunable UV wavelengths.

The CLBO crystal is critically phase-matched and is set in an oven to maintain a temperature above 150°C to prevent hygroscopic crystal damage.

The CLBO crystal was angle tuned to provide the best possible phase match to generate maximum fourth harmonic 263-nm energy. With an input of approximately 9 mJ of 527-nm pump energy, the CLBO crystal produced a maximum of 0.470 mJ of 263-nm energy. The fourth harmonic 263-nm conversion efficiency was approximately 5%. According to design specifications, approximately 9 mJ of 527-nm energy should produce 1.5 mJ of 263-nm energy. At the time of the test, visible clouding occurred within the CLBO crystal which created imperfections and thereby reduced the transparency of the crystal. The imperfections in the CLBO crystal increased the absorption and scattering of the 527-nm energy thus reducing the amount of 263-nm energy generated. This CLBO crystal should be replaced with a 15-mm long crystal to generate more fourth harmonic wavelength. This will allow

an increase in the conversion efficiency of the fourth harmonic energy to pump the Ce:LiCAF.

The fourth harmonic 263-nm energy is used to pump the Ce:LiCAF crystal to produce tunable UV wavelengths used in DIAL measurements. The Ce:LiCAF crystal requires a threshold energy of approximately 460  $\mu\text{J}$  – 500  $\mu\text{J}$  to produce tunable UV wavelengths. With a maximum availability of fourth harmonic energy of 470  $\mu\text{J}$ , numerous attempts were made to produce tunable UV wavelengths from the Ce:LiCAF, however, no UV wavelengths were generated. After numerous attempts, it shows that the maximum available fourth harmonic energy of 470  $\mu\text{J}$  is insufficient to produce tunable UV wavelengths. Nevertheless, with a new CLBO crystal- generating, higher, fourth- harmonic pump energies to pump the Ce:LiCAF crystal, tunable UV wavelengths can be produced.

To test the receiver and data acquisition system, an atmospheric test was conducted by transmitting the 527-nm energy into the atmosphere to detect aerosols. The backscattered return was collected by the telescope and sent through the receiver system to the APD. From the APD, the data acquisition system received the backscattered signal and processed the data. The receiver and data acquisition system worked as accepted and no issues were experienced. Additionally, the lidar receiver from the telescope fiber optic to the APD was measured with an optical efficiency of 43% (including filter).

The maximum sampling rate of the NI-DAQ boards for the aerosol channel (527-nm) is 10 MS/s per channel, also known as the digitizing rate. In addition, the FWHM of the 527-nm wavelength is 107-ns which is used to determine the effective spatial pulse length. Therefore, the maximum resolution of the aerosol channel is determined by the FWHM of the 527-nm wavelength.

An atmospheric test was conducted on January 8, 2009 by transmitting the 527-nm beam into the atmosphere. The daytime conditions were overcast with low-lying clouds. The graph of the results showed a boundary layer and cloud return at an altitude of approximately 500 m. Moreover, the same graph illustrated complete overlap of the transmitted beam and the telescope's field-of-view occurred at approximately 150 m.

Theoretical calculations were computed to compare measured and theoretical returns of the lidar equation. The backscattered coefficients were calculated using equation (41) as discussed in chapter 4. The calculation considers molecular scattering only. Also, the extinction coefficients were calculated using equation (44) and only considers molecular scattering. For reference, the lidar equation is again shown in equation (48) with the lidar constants used in the theoretical lidar calculation listed in table 2.

$$P(R) = P_0 \beta(\lambda, \theta, R) \frac{c \tau}{2} \frac{A}{R^2} \eta(\lambda) G(R) T^2(\lambda, R) \quad (48)$$

Table 3: Lidar equation values.

Lidar Parameters	Value
Power transmitted, $P_0$	86262 W
Backscatter Coefficient, $\beta(\lambda, \theta, R)$	Refer to Eq. (41)
Effective spatial pulse length, $c\tau/2$	16 m
Telescope Area, $A$	$0.50 \text{ m}^2$
Receiver Efficiency, $\eta(\lambda)$	0.43
Overlap, $G(R)$	1
Extinction Coefficient, $T^2(\lambda, R)$	Refer to Eq. (44)

A point of reference was determined in order to provide an accurate comparison between the measured and calculated lidar return signal. The point of reference for comparison is in front of the APD. The area before the detector receives the signal. The APD data acquisition system provides raw data in units of voltage. In order to determine the power received by the APD, a conversion factor of 5 MV/W as measured in section 5.3 was used to convert the raw data into units of power. The theoretical calculation determined the return signal to the same point of reference.

A graph of the measured results of the transmitted 527-nm visible beam and theoretical results of the lidar equation is shown in figure 29. Both the measured and theoretical results show good agreement. Since the theoretical result is based on molecular scattering only and aerosol scattering is not calculated, the calculated result is expected to have slightly less power return.

Alternatively, the measured result has a higher power return due to additional scattering from aerosols normally found within the boundary layer. The result of the comparison between the measured and theoretical indicates the lidar 527-nm aerosol channel is providing accurate lidar returns and can be used for atmospheric analysis.

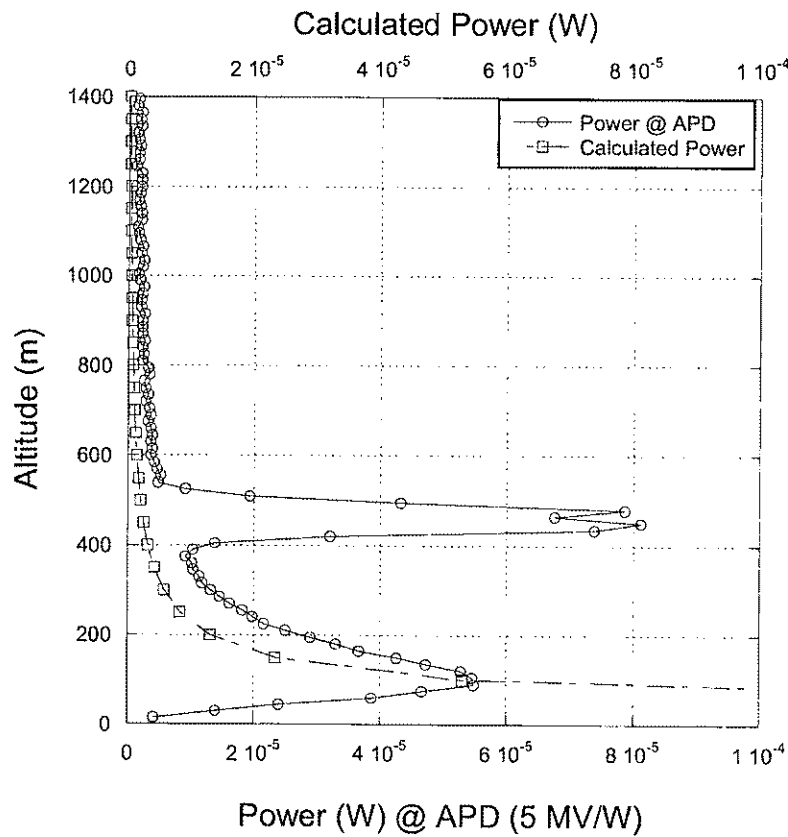


Figure 29: Comparison of the theoretical and experimental results.

Future work would include replacing the existing 10-mm CLBO crystal with a 15-mm CLBO crystal. This will provide a higher conversion efficiency of the 527-nm pump energy to the fourth harmonic 263-nm energy. The higher conversion efficiency will provide more fourth harmonic 263-nm energy to pump the Ce:LiCAF crystal. With sufficient 263-nm energy pumping the Ce:LiCAF crystal, tunable UV wavelengths will be produced. In turn, these wavelengths can be used for DIAL ozone measurements.



## CHAPTER VII

### CONCLUSIONS

In this thesis, a compact lidar for aircraft ozone atmospheric measurements was tested and evaluated. Each of the major subsystems was characterized and from the results the subsystems were optimized for maximum efficiency.

The laser transmitter was tested to evaluate the amount of laser energy produced. The laser pump produced a maximum of 9.23 mJ of 527-nm energy to pump the CLBO crystal to generate fourth harmonic 263-nm energy. The 527-nm laser pump provided sufficient energy to pump the CLBO crystal. However, due to the condition of the CLBO crystal, an inadequate amount of the 263-nm energy was produced. Attempts were made to pump the Ce:LiCAF crystal, however, no tunable UV wavelengths for DIAL ozone measurements were achieved.

The visible 527-nm energy was transmitted into atmospheric and the backscattered results were collected by the receiver system and processed by the data acquisition system. The aerosol channel has a maximum resolution determined by the FWHM of the 527-nm wavelength. Both the receiver and data acquisition system operated as expected.

Atmospheric measurements were conducted by transmitting the 527-nm into the atmosphere and the backscattered results were evaluated. In addition,

theoretical calculations were performed based on the parameters of the lidar system and a lidar equation result was produced. Both the measured results and theoretical results of the lidar equation showed good agreement. As expected, the measured results indicated a slightly higher return signal due to additional scattering from aerosols within the boundary layer. With this comparison, the lidar 527-nm aerosol channel is performing as expected.

The next step would require the replacement of the 10-mm CLBO crystal with a 15-mm crystal. Using the 527-nm energy to pump the 15-mm CLBO crystal will provide sufficient generation of fourth harmonic 263-nm energy to pump the Ce:LiCAF to produce tunable UV wavelengths. Future work would include characterizing the Ce:LiCAF laser for the energy produced within the tunable range of UV wavelengths. The tunable UV wavelengths would be able to provide DIAL atmospheric ozone measurements.

## REFERENCES

1. Gary Morris, Stratospheric Ozone: Morphology of Ozone, [http://www.ccpo.odu.edu/SEES/ozone/class/Chap\\_3/](http://www.ccpo.odu.edu/SEES/ozone/class/Chap_3/)
2. Richard P. Turco, *Earth Under Siege*, Oxford University Press, New York (1997).
3. J. Hornstein, E. Shettle, R. Bevilacqua, S. Chang, E. Colon, L. Flynn, E. Hilsenrath, S. Mango, H. Bloom, and F. Sanner, "The Ozone Mapping and Profiler Suite-Assimilation Experiment (OMPS-AE)," *Geoscience and Remote Sensing Symposium 2*, 809-811 (2002).
4. Mohamed A. El-Sharkawi, *Electric Energy*, CRC Press, New York (2005).
5. S. McDermid, S. Godin, and L. Lindqvist, "Ground-based laser DIAL system for long-term measurements of stratospheric ozone," *Applied Optics* **29**(25), 3603-3612 (1990).
6. H. Gao and D. Niemeir, "Using functional data analysis of diurnal ozone and NO<sub>x</sub> cycles to inform transportation emissions control," *Science Direct* **13**, 221-238 (2008).
7. J. Snow, J. Dennison, D. Jaffe, H. Price, J. Vaughan, B. Lamb, "Aircraft and surface observations of air quality in Puget Sound and a comparison to a regional model," *Atmospheric Environment* **37**, 4019-4032 (2003).
8. N. Vasa, M. Uchiumi, and S. Yokoyama, "Application of Differential Lidar System for CO<sub>2</sub> Monitoring at Different Wavelengths around 1.6  $\mu\text{m}$  and 2  $\mu\text{m}$ ," *Proceedings of the SPIE* **6409**, 640909 (2006).
9. J. Reagan, M. McCormick, and J. Spinhirne, "Lidar Sensing of Aerosols and Clouds in the Troposphere and Stratosphere," *Proceedings of the IEEE* **77**(3), 433-448 (1989).
10. E. Browell, "Differential Absorption Lidar Sensing of Ozone," *Proceedings of the IEEE* **77**(3), 419-432 (1989).
11. TOMS - <http://toms.gsfc.nasa.gov/>

12. V. Kovalev and W. Eichinger, *Elastic Lidar*, John Wiley & Sons, Inc., New Jersey (2004).
13. C. Weitkamp, *Lidar*, Springer, New York, (2005).
14. J. Aparna, S. Satheesh, and V. Mahadevan, "Determination of aerosol extinction coefficient profiles from LIDAR data using the optical depth solution method," *Proceedings of the SPIE* **6408**, 64080 (2006).
15. W. Richter, "Optical Design for Lidar," *Proceedings of the SPIE* **2505**, 197-204 (1995).
16. G. Gimmetstad, E. Patterson, D. Roberts, J. Stewart, L. West, and J. Wood, "A Next-Generation Ground-based Sensor for Tropospheric Ozone," *Geoscience and Remote Sensing Symposium* **3**, 1026-1028 (2001).
17. Z. Wang, H. Hu, J. Zhou, and Z. Gong, "Three-wavelength dual-DIAL method for ozone measurements," *Proceedings of the SPIE* **2831**, 268-277 (1996).
18. E. Browell, "Airborne Lidar Measurements of Ozone, Water Vapor, and Aerosols in Large-Scale Atmospheric Studies," *Geoscience and Remote Sensing Symposium* **2**, 865- 868 (1993).
19. A. Jones, R. De Young, and H. Elsayed-Ali, "Compact Ozone Differential Absorption Lidar (DIAL) Transmitter Using Solid-State Dye Polymers," *NASA Langley Technical Report Server*, (2001).
20. T. Sudmeyer, Y. Imai, H. Masuda, N. Eguchi, M. Saito, and S. Kubota, "Efficient 2<sup>nd</sup> and 4<sup>th</sup> harmonic generation of a single-frequency, continuous-wave fiber amplifier," *Optics Express* **16**(3), 1546-1551 (2008).
21. W. Koechner, *Solid-State Laser Engineering*, Springer, New York (1999).
22. J. Meyn and M. Fejer, "Tunable ultraviolet radiation by second-harmonic generation in periodically poled lithium tantalate," *Optic Letters* **22**(16), 1214- 1216 (1997).
23. P. Franken, A. Hill, C. Peters, and G. Weinreich, "Generation of Optical Harmonics," *Physical Review Letters* **7**(4), 118-120 (1961).

24. Robert Boyd, *Nonlinear Optics*, Academic Press (1992).
25. V.G. Dmitriev, G.G. Gurzadyan, and D. N. Nikogosyan, *Handbook of Nonlinear Optical Crystals*, Springer, New York (1995).
26. Y.R. Shen, *The Principles of Nonlinear Optics*, John Wiley & Sons, Inc., New York (1984).
27. *An Ozone DIAL Transmitter Module for Airborne Applications*, Science & Engineering Services, Inc., (2006).
28. C. Marshall, S. Payne, J. Speth, J. Tassano, and W. Krupke, "Properties of Ce:LiSrAlF<sub>6</sub> and Ce:LiCaAlF<sub>6</sub> ultraviolet lasers," *Proceedings of the SPIE* **2115**, 7-18 (1994).
29. LidarPC program Manual
30. E.D. Hinkley, *Laser Monitoring of the Atmosphere*, Springer, New York (1976).
31. L. Elterman, "UV, Visible, and IR Attenuation for Altitudes to 50 Km," *Air Force Cambridge Research Laboratories, Environmental Research Paper* 285 (1968).
32. K. Marase, M. Yoshimura, T. Kamimura, K. Nakai, Y. Mori, and T. Sasaki, "Fourth harmonic generation of a high-repetition rate Nd:YAG laser in CsLiB<sub>6</sub>O<sub>10</sub> crystal," *Lasers and Electro-Optic* **99**, 451-452 (2000).

## VITA

**NAME:** Joel A. Marcia

### DEGREES:

Master of Science (Electrical Engineering), Old Dominion University,  
Norfolk, Virginia, May 2009

Bachelor of Science (Electrical Engineering), Old Dominion University,  
Norfolk, Virginia, May 2007

Associate of Science (Engineering), Tidewater Community College,  
Virginia Beach, August 2005

### EXPERIENCE:

NASA, Hampton, VA August 2007 – present  
Masters Thesis Research

NASA, Hampton, VA August 2006 – December 2006  
Laser System Project

### PUBLICATION:

J. Marcia and R. De Young, "Compact Ozone Lidar For Atmospheric Ozone and Aerosol Measurements," *NASA Technical Memorandum 2007-214544* (2007).

### GRANTS AND CONTRACTS AWARDED:

Virginia Space Grant Consortium Graduate Fellowship

### PROFESSIONAL SOCIETY MEMBERSHIP:

Eta Kappa Nu, Electrical and Computer Honor Society